



5-2007

Design and Analysis of a General Purpose Operational Amplifier for Extreme Temperature Operation

Chandradevi Ulaganathan
University of Tennessee - Knoxville

Follow this and additional works at: https://trace.tennessee.edu/utk_gradthes



Part of the [Electrical and Computer Engineering Commons](#)

Recommended Citation

Ulaganathan, Chandradevi, "Design and Analysis of a General Purpose Operational Amplifier for Extreme Temperature Operation. " Master's Thesis, University of Tennessee, 2007.
https://trace.tennessee.edu/utk_gradthes/327

This Thesis is brought to you for free and open access by the Graduate School at TRACE: Tennessee Research and Creative Exchange. It has been accepted for inclusion in Masters Theses by an authorized administrator of TRACE: Tennessee Research and Creative Exchange. For more information, please contact trace@utk.edu.

To the Graduate Council:

I am submitting herewith a thesis written by Chandradevi Ulaganathan entitled "Design and Analysis of a General Purpose Operational Amplifier for Extreme Temperature Operation." I have examined the final electronic copy of this thesis for form and content and recommend that it be accepted in partial fulfillment of the requirements for the degree of Master of Science, with a major in Electrical Engineering.

Benjamin J. Blalock, Major Professor

We have read this thesis and recommend its acceptance:

Charles L. Britton, Syed K. Islam

Accepted for the Council:

Carolyn R. Hodges

Vice Provost and Dean of the Graduate School

(Original signatures are on file with official student records.)

To the Graduate Council:

I am submitting herewith a thesis written by Chandradevi Ulaganathan entitled "Design and Analysis of a General Purpose Operational Amplifier for Extreme Temperature Operation." I have examined the final electronic copy of this thesis for form and content and recommend that it be accepted in partial fulfillment of the requirements for the degree of Master of Science, with a major in Electrical Engineering.

Benjamin J. Blalock, Major Professor

We have read this thesis
and recommend its acceptance:

Charles L. Britton

Syed K. Islam

Accepted for the Council:

Carolyn Hodges

Vice Provost and Dean of the Graduate
School

(Original signatures are on file with official student records.)

**DESIGN AND ANALYSIS OF A GENERAL PURPOSE
OPERATIONAL AMPLIFIER FOR EXTREME TEMPERATURE
OPERATION**

A Thesis Presented for the
Master of Science Degree
The University of Tennessee, Knoxville

Chandradevi Ulaganathan
May 2007

*This thesis is dedicated to my parents,
Smt. Saroja Ulaganathan and Shri. Ulaganathan,
my friend Aparna Thyagarajan and the rest of my family
for always inspiring and encouraging me to see my dreams come true*

ACKNOWLEDGEMENTS

I would like to express my sincere gratitude to my advisor Dr. Benjamin J. Blalock whose constant guidance, support and patience helped me in completing this thesis. I wish to thank my thesis committee members Drs. Charles L. Britton and Syed K. Islam for their helpful suggestions and support in this work.

I am especially grateful to Dr. Dayakar Penumadu for offering invaluable guidance and financial support in the initial stage of my Masters work. I would like to thank all my colleagues in the Integrated Circuits and Systems Laboratory (ICASL) for their support. I am indebted to Neena Nambiar and Suheng Chen for the priceless discussions, suggestions and their inspiration.

I thank my parents Smt. Saroja Ulaganathan and Shri. Ulaganathan, and my sisters Aarthi and Vaishnavi, for their unconditional support and faith in me. I am grateful to my friends – Aparna, Sangeetha, Ezhil, Juhee, Anton and others for their support and encouragement.

This work was funded by the NASA Exploration Technology Development Program (ETDP). Special appreciation is extended to our collaborators, including Prof. John Cressler's team at Georgia Tech.

ABSTRACT

Operational amplifiers (op amps) are key functional blocks that are used in a variety of analog subsystems such as switched-capacitor filters, analog-to-digital converters, digital-to-analog converters, voltage references and regulators, etc. There has been a growing interest in using such circuits for "extreme environment" electronics, in particular for electronics capable of operating down to deep-cryogenic temperatures for lunar and Martian surface explorations.

This thesis presents the design and analysis of a general purpose op amp suited for "extreme environment" applications, with a wide operating temperature range of 93 K to 398 K. The op amp has been implemented using a CMOS architecture to exploit the low temperature operational advantages offered by MOS devices, such as increase in carrier mobility, increased transconductance, and improved switching speeds. The op amp has a two-stage architecture to provide high gain and also incorporates common-mode feedback around the input stage. Tracking compensation has been implemented to provide stable frequency compensation over wide temperature. The op amp has been fabricated in a commercial 0.35- μm 3.3-V SiGe BiCMOS process. The op amp has been tested for the temperature range of 93 K to 398 K and is unity-gain stable and fully functional over this range.

This thesis begins with a study of the impact of temperature on MOS devices and operational amplifiers. Next, the design of the wide temperature general-purpose operational amplifier is presented along with an analysis of the common-mode feedback circuit. The op amp is then characterized using simulation results. Finally, the test setup is presented and the measurement results are compared with those from simulation.

TABLE OF CONTENTS

CHAPTER 1	INTRODUCTION.....	1
1.1	Motivation	1
1.2	Scope of the Thesis.....	2
1.3	Organization of the Thesis.....	3
CHAPTER 2	IMPACT OF TEMPERATURE ON ELECTRONICS.....	4
2.1	Operational Amplifiers – Fundamentals	4
2.2	Effect of Temperature Variation	5
2.2.1	Effect on MOS devices	5
2.2.2	Effect on Op amp circuits	12
CHAPTER 3	DESIGN OF THE WIDE TEMPERATURE RANGE GENERAL- PURPOSE OP AMP	14
3.1	Op amp Architecture	14
3.1.1	Input Stage	14
3.1.2	Output Stage.....	16
3.2	Complete Schematic.....	18
3.2.1	Open-loop Gain.....	19
3.2.2	Frequency Compensation.....	20
3.2.3	Input common mode range	22
3.2.4	Noise	23
3.2.5	Offset Voltage.....	24
3.2.6	Output Swing	26
3.2.7	Slew Rate	26
3.2.8	Common-mode Feedback (CMFB)	27
3.2.9	Current Reference	32
3.3	Simulation Results.....	33
3.4	Layout and Implementation.....	40

CHAPTER 4	WIDE TEMPERATURE RANGE GENERAL-PURPOSE OP AMP – MEASUREMENT RESULTS	42
4.1	Temperature Testing.....	42
4.2	Test Setup.....	43
4.3	Summary.....	57
CHAPTER 5	CONCLUSIONS	58
5.1	Conclusions	58
5.2	Future Work.....	58
5.2.1	Circuit-level	58
5.2.2	System-level.....	59
REFERENCES	60
APPENDIX	65
A.1	Calculation of Open-loop Gain	66
A.2	Calculation of Input Referred Noise Voltage.....	67
A.3	Derivation of the Loop Gain of CMFB Circuit.....	69
A.4	Test Board	72
VITA	73

TABLE OF TABLES

Table 1.1 - Op amp Specifications.....	3
--	---

TABLE OF FIGURES

Figure 2.1 - Basic operational amplifier	5
Figure 2.2 - Simple two-stage CMOS op amp.....	12
Figure 3.1 - Input stage of the op amp	15
Figure 3.2 - The output stage along with input stage and CMFB block diagram [28]	16
Figure 3.3 - Complete schematic of the op amp	19
Figure 3.4 - Common-mode feedback circuit along with the input stage.....	28
Figure 3.5 - Simulated frequency response of CMFB circuit.....	30
Figure 3.6 - CMFB transient response for (a) common-mode signal and (b) differential-mode signal.....	31
Figure 3.7 - Plot showing the difference voltage at output of input stage vs. bias current.....	32
Figure 3.8 - Schematic of constant IC current reference circuit [35]	33
Figure 3.9 - Simulation result for ICMR across temperature	34
Figure 3.10 - Simulation result for open-loop gain and phase across temperature.....	35
Figure 3.11 - Simulation result for small-signal rise time across temperature	35
Figure 3.12 - Simulation result for small-signal fall time across temperature.....	36
Figure 3.13 - Simulated positive slewing edge across temperature.....	36
Figure 3.14 - Simulated negative slewing edge across temperature.....	37
Figure 3.15 - Simulated input referred noise voltage across temperature	38
Figure 3.16 - Simulation result for PSRR across temperature.....	38
Figure 3.17 - Simulation result for CMRR across temperature	39
Figure 3.18 - Simulation result for constant IC current reference	39
Figure 3.19 - Layout of the general-purpose op amp.....	41
Figure 3.20 - Die photo of the general-purpose op amp	41
Figure 4.1- Setup for temperature testing	42
Figure 4.2 - Measurement setup for offset voltage	44
Figure 4.3 - Measured V_{OS} across temperature.....	44
Figure 4.4 - Measurement setup for ICMR.....	45
Figure 4.5 - Measured ICMR max across temperature.....	46
Figure 4.6 - Open-loop gain measurement circuit	47
Figure 4.7 - Measured results for open-loop gain across temperature.....	47
Figure 4.8 - Measured UGBW across temperature.....	49
Figure 4.9 - Measured UGBW across temperature using sinusoidal input signal	49
Figure 4.10 - Measured phase margin across temperature	50
Figure 4.11 - Measured positive slewing edge across temperature	51
Figure 4.12 - Measured negative slewing edge across temperature	51
Figure 4.13 - Measured slew rate across temperature.....	52
Figure 4.14 - Setup for noise measurement	53
Figure 4.15 - Measured input referred noise voltage across temperature.....	53
Figure 4.16 - PSRR measurement circuit	54
Figure 4.17 - Measured PSRR across temperature	55
Figure 4.18 - CMRR measurement circuit.....	56
Figure 4.19 - Measured CMRR across temperature	56
Figure 4.20 - Measured bias current vs. temperature.....	57

Figure A.1 - Setup to determine the flicker noise corner frequency.....	67
Figure A.2 - Small-signal equivalent of the CMFB's ac half-circuit	70
Figure A.3 - Picture of Test Board.....	72

Chapter 1 Introduction

1.1 Motivation

Operational amplifiers (op amps) are versatile devices used as key functional blocks in a variety of high-precision analog/mixed-signal systems. Its application spans the broad electronic industry filling requirements for signal conditioning, special transfer functions, analog instrumentation, analog computation and special systems design [1]. There continues to be a growing interest in developing SoC (System-on-Chip) integrated systems for use in numerous applications. These applications often place challenging constraints in the design of various electronic components. “Extreme environments” represent a class of niche electronic applications wherein the electronic components must operate in an environment that is outside the domain of commercial or military specifications. This would include temperatures above or below the standard military specification, in a radiation intensive environment such as space, in a high vibration environment, in a high (low) pressure environment, or even in a caustic or chemically corrosive environment as inside the human body [2].

In this thesis, extreme temperature effects on electronics have been studied and a robust operational amplifier that works across a wide temperature range has been designed, fabricated and tested. With the recent development of low temperature electronics to support space exploration, this work is targeted at the moon’s surface environment where the ground temperature swings up to 393 K (120 °C) during the day and down to 93 K (-180 °C) during the night.

At present, robotic exploration rovers [3] have all the essential parts that control the system, such as electronics, batteries and computers operating in a temperature controlled environment of a warm electronic box (WEB). The temperature in the WEB is maintained to be within the operating range of all the enclosed components in order to guarantee their reliable operation. Heaters, thermostats, heat switches and gold paint help maintain the temperature inside the WEB, but they increase the system’s power consumption, size and mass [3]. The use of warm boxes also mandates a centralized

architecture wherein the control signals are generated in the WEB and communicated to various parts of the rover through wiring cables, thus reducing reliability. By developing electronic components that are capable of reliable operation under extreme conditions without a “warm box”, a distributed architecture can be realized. The result would be reduced power consumption and the launch weight while the reliability, vehicle form factor, safety and mission cost are also dramatically improved [4].

With this motivation, the goal of this work is to develop an operational amplifier that functions well under extreme temperatures. This would help in designing remote electronic systems for robotic rovers and other spacecraft that provide data acquisition and control for various applications.

1.2 Scope of the Thesis

The purpose of this work is to design an operational amplifier that can operate in extreme environments. Specifically, the op amp is targeted to serve as a general purpose building block in high-precision analog signal conditioning systems. There are several parameters that characterize an op amp. Some key parameters include gain, gain-bandwidth, slew rate, input common-mode range (ICMR), common-mode rejection ratio (CMRR), power-supply rejection ratio (PSRR), output swing, offset voltage, noise and power consumption. Depending on the system specification, some characteristics are given more precedence over others. For this work, it is important that the gain, gain-bandwidth, output swing, noise and offset voltage are maintained at an acceptable level across temperature. The op amp is fabricated in a 0.35- μm 3.3-V SiGe BiCMOS process. Table 1.1 presents a list of requirements set for the design of this general purpose op amp. An all-CMOS approach is used for this work to provide the opportunity to study and analyze the impact of temperature variation on MOS devices and its influence on op amp performance. An analysis of the common-mode feedback circuitry implemented in the differential input stage of the op amp is also performed.

Table 1.1 - Op amp Specifications

Parameter	Specification
I_{DD}	$< 2 \text{ mA}$
Gain Bandwidth	$> 1 \text{ MHz}$
Capacitive Load	50 pF
$ICMR_{MIN}$	0 V
Slew Rate	$> 2 \text{ V}/\mu\text{sec}$
V_{OS}	$< 10 \text{ mV}$
e_{ni} at 100 KHz	$< 100 \text{ nV}/\sqrt{\text{Hz}}$
O/P swing for $ I_{LOAD} = 0.3 \text{ mA}$	$\geq (0.2 \rightarrow 3.1) \text{ V}$

1.3 Organization of the Thesis

Chapter 2 starts with a brief review of op amps. This is followed by a discussion on the influence of temperature on the operation of MOS devices, circuits and the constraints set on the design of extreme temperature op amps.

Chapter 3 provides an in-depth look at the design of the general-purpose op amp. The common-mode feedback circuit, the frequency compensation technique and current reference circuit are discussed. Then, the op amp is characterized using simulation results.

Chapter 4 presents the measured results from the fabricated op amp and also describes the test setup used for each measurement. The measured results are compared with the theoretical and simulated results.

Chapter 5 provides conclusion and the thesis ends with a discussion of possible enhancements and future work.

Chapter 2 Impact of Temperature on Electronics

Chapter 2 presents a discussion on the effects of temperature on MOS devices and op amp circuit performance. This discussion begins with briefly reviewing the essential components that make up an op amp and characterizing an op amp using the parameters that dictate its performance.

2.1 Operational Amplifiers – Fundamentals

Ideal operational amplifiers are functional blocks that have infinite voltage gain over an infinite bandwidth, infinite input resistance and zero output resistance. In practice, op amps only approach these ideal characteristics. They use negative feedback to establish and control a closed-loop transfer function that is stable and independent of the open-loop gain of the op amp. Figure 2.1 presents a functional block diagram of a basic operational amplifier. The differential input stage provides the required high gain for the op amp and can also perform the differential-input to single-ended output conversion. The second stage is usually an inverting stage and can offer high gain as well as differential-to-single ended conversion if necessary. Op amps that need to drive small resistive loads also include a buffer/output stage that drives the load and determines the output swing. The compensation circuitry ensures frequency stability when the op amp is used in a negative feedback network. The biasing circuitry provides a stable, quiescent operating point for the entire circuit. Op amps with different levels of complexity are used in many applications and it is important to understand the parameters used in evaluating these op amps. A brief review of the op amp parameters is included here.

The dynamic range of an op amp is controlled by the op amp's offset voltage, noise, input common-mode range (ICMR) and output swing. The ability of the op amp to provide an accurate closed-loop gain is dictated by the open-loop gain (A_{OL}). The frequency response of the circuit is characterized by the small-signal bandwidth, phase

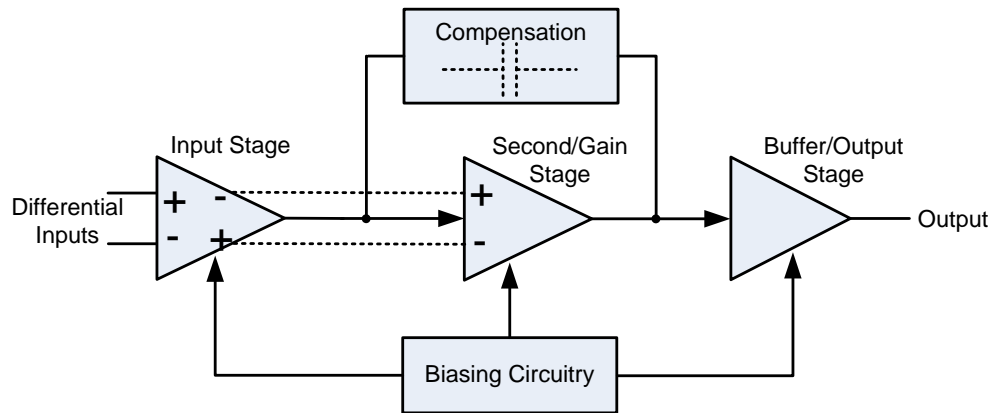


Figure 2.1 - Basic operational amplifier

margin, settling time and also large signal bandwidth. The range of maximum and minimum voltages that can be obtained without any clipping at the output is represented as output swing. Slew Rate is the maximum rate at which the output voltage can change. The ability of an op amp to prevent its output from being affected by any variation in the power supply voltage is characterized as PSRR. The factors that influence these parameters are examined in detail in the subsequent chapters.

2.2 Effect of Temperature Variation

A good understanding of the operation of MOS devices and op amp circuits when subjected to temperature variation is essential in designing an op amp to function at extreme temperatures. This section briefly discusses the behavior of MOSFET devices and its effect on op amp circuits at extreme temperature conditions.

2.2.1 Effect on MOS devices

2.2.1.1 Low Temperature (LT) behavior

The operation of semiconductor devices at cryogenic temperatures has been studied extensively for the past 3 decades because of the possibility of providing significant performance improvement at low temperature. Some of the notable advantages offered by low temperature operation include steeper subthreshold slope,

substantial increase in carrier mobility and saturation velocity, higher transconductance, reduced thermal noise, increased thermal conductivity, improved reliability through latch-up immunity, decrease in leakage current, and reduction of thermally activated failure processes [8, 9, 10]. Operation at low temperature is challenged by the increase in threshold voltage, increased susceptibility to hot carrier degradation effects and impurity carrier freeze-out resulting in kink phenomenon and transient behavior of drain current at cryogenic temperatures [10].

2.2.1.2 High Temperature (HT) behavior

Study of high temperature electronics is mainly driven by industrial applications in geothermal sensors, space exploration and aircraft/automobile engine monitors [18 - 21]. The limitations of HT operation are primarily due to lowering of mobility and thus a reduction in transconductance, increase in leakage currents, latch-up and reduced reliability of the oxide layer, metal interconnects and packaging [22].

The parameters that are altered due to temperature variation have a major influence on device performance. These parameters are discussed here.

2.2.1.3 Threshold Voltage variation

A standard expression for MOSFET threshold voltage is [5, 12]

$$V_{TH} = 2\phi_F + \phi_{ms} - \frac{Q_{SS}}{C_0} \mp \sqrt{\frac{2\varepsilon_{Si}qN_{SUB}(2\phi_F)}{C_{OX}}} \quad (2.1)$$

where ϕ_F is the Fermi potential, ϕ_{ms} is metal-semiconductor work function difference, Q_{SS} is the extrinsic charge due to surface states, interface energy states, oxide traps etc. , C_{OX} is the gate oxide capacitance, N_{SUB} is the substrate doping concentration, ε_{Si} is the dielectric concentration of silicon, q is the electron charge.

N_{SUB} , ϕ_{ms} , Q_{SS} , C_{OX} are independent of temperature and the Fermi potential is represented as [5, 12]

$$\phi_F = \frac{kT}{q} \ln \left[\frac{N_{SUB}}{n_i} \right] \quad (2.2)$$

which is dependent on temperature. With a reduction in temperature, the intrinsic carrier concentration, n_i , reduces and the Fermi potential, ϕ_F , increases, hence the threshold voltage increases at LT. In analog circuits the increase in V_{TH} at LT reduces the dynamic range of the circuit. Thus in an op amp, the ICMR would be reduced [13]. For the BiCMOS fabrication process used here, the V_{TH} of NMOS and PMOS devices vary approximately 200 mV across the temperature range of -180°C to 125°C .

2.2.1.4 Mobility Variations

The carrier mobility variation across temperature presents a major constraint on circuits operating across extreme temperature ranges. At LT mobility may increase by a factor of 4 to 6, while at HT mobility decreases. The factors controlling mobility would help in understanding this temperature dependence. The carrier mobility μ is controlled by various scattering mechanisms like lattice scattering, ionized impurity scattering and vertical field dependent surface scattering [14]. These mechanisms, and thus μ are a function of applied electric field, temperature, channel impurity concentration and the oxide layer thickness.

At room temperature, for small gate voltages, surface scattering is relatively unimportant, so the surface mobility can approach bulk mobility. As gate voltage increases, inversion layer carriers are subjected to increased electric field and are pushed toward the surface, causing surface scattering to become more significant and lowers mobility [14].

As temperature is lowered to near liquid nitrogen temperature (LNT) of about 77 K, the reduction in the lattice vibration makes lattice scattering less significant. Therefore, mobility increases with reduction in temperature. The extent of this enhancement depends on other factors influencing mobility. For instance, in transistors with light doping near the surface, surface scattering effects dominate and mobility depends strongly on vertical field applied. For such devices, the enhancement in mobility at LNT over 27°C is large for low vertical fields and less for higher fields [14]. Also, devices built in wells are expected to have lower mobility at all temperatures and less μ enhancement since ionized impurity scattering, which is independent of the magnitude of

vertical field, is significant at all temperatures [14].

The dependence of mobility as a function of temperature can be represented as [10]

$$\mu = \mu_0 \left[\frac{T}{T_0} \right]^{-\alpha} \quad (2.3)$$

where α is a constant that describes the temperature dependence and approximated as 1.3 for electrons and 1.2 for holes for a 0.5- μm CMOS technology.

The transconductance, g_m , for inversion-mode MOSFETs is proportional to the drift velocity in the channel and thus to the carrier mobility. Therefore, the variations in μ across temperature affect the transconductance and thus the gain and bandwidth of circuits.

2.2.1.5 Noise

The chief sources of noise in MOSFET devices are thermal noise and flicker noise. Thermal noise is due to the effective resistance of the channel and is directly dependent on the temperature of operation. The thermal noise can be represented as an input-referred PSD as [5]

$$e_{ni}^2 = 4kT \left(\frac{2}{3} \right) g_m \quad (2.4)$$

Thus, at LT the thermal noise can be significantly reduced, while at HT thermal noise increases and thereby affects the dynamic range of circuits.

Flicker noise source is attributed to trapping levels along the Si-SiO₂ interface in the channel. This noise is larger than thermal noise for frequencies below 1 to 10 KHz for most bias conditions and device geometries [5]. The gate-referred PSD of flicker noise is given as [14]

$$e_{nif}^2 = \frac{K_1}{C_{ox}WLf} \quad (2.5)$$

where K_1 is a constant that is dependent on surface conditions and is dependent on temperature. At very LT, the increase in gate injection current, due to hot-carrier effects, results in an increase in oxide trapped charge and so flicker noise may actually increase

slightly [15]. Hence for low frequency applications where flicker noise is dominant, the noise might not always reduce with a decrease in temperature. At HT there is an increase in the thermal as well as the flicker noise.

2.2.1.6 Subthreshold Operation

In switching circuits, the variation of drain current with gate voltage in the subthreshold region is important in order to maintain the off current and control the switching characteristics. The variation is referred to as subthreshold slope and is represented as [10]

$$S = \frac{d(\log I_{DS})}{dV_G} = \frac{q}{2.3kT} \left(\frac{C_{OX}}{C_{OX} + C_{Si} + C_{SS}} \right) \quad (2.6)$$

where k is Boltzmann's constant, T is the absolute temperature, C_{OX} is the gate-oxide capacitance, C_{Si} is the silicon capacitance at the source boundary, and C_{SS} is the capacitance associated with charging and discharging interface traps. The capacitances do not vary much with temperature, but the subthreshold slope S depends on the temperature. It has been shown [10] that the typical values of S improved by a factor of 4 at 77 K when compared to the room temperature value. Thus at LT, the subthreshold slope is steep requiring a small voltage change to cause a large change in current (e.g., "off" to "on").

2.2.1.7 Reliability

The reliability of CMOS devices is a strong function of operating voltage and temperature [10]. At LT, the mechanisms that cause failure such as latch up, electro-migration, oxide breakdown are reduced, thus improving the reliability. But at HT, these failure mechanisms dominate and thereby affect the reliable operation of devices.

Latch-up is due to the presence of parasitic bipolar transistor structures formed within the process cross section. The parameters that control latch-up such as holding current, holding voltage, and trigger current depend on the current gain β of the parasitic transistors and on the forward base-emitter voltages and are therefore dependent on temperature [23]. Latch-up can be triggered by transient current flow and would cause

failure by the positive feedback action in the parasitic BJTs [16]. At LT the gain of BJTs is very low such that the total gain in the parasitic BJTs is less than unity and thus latch-up is suppressed. But at HT the increase in β enhances the likelihood of latch-up to occur.

Electro-migration, caused by the creation of metal voids and shorts in metal interconnects due to the movement of metal atoms at high current densities, has a thermal activation process. So at LT electro-migration is significantly reduced, but at HT electro-migration reduces reliable circuit operation.

Hot carrier degradation effects: When high electric field is applied, the carriers gain high kinetic energy and may be injected into the gate oxide and become trapped there. This changes the MOSFET's threshold voltage and transconductance. At LT the reduced lattice scattering due to lattice vibrations results in a large fraction of carriers reaching the gate and a high susceptibility to hot carrier degradation. At -180 °C (77 K), there is an increase in these effects. This augmentation is not due to the enhanced trapping in oxide, but due to increased influence of trapped charge on device operation [10]. The degradation can be controlled by operating the devices with lower voltages and thus placing a design constraint on the gate voltage [10].

2.2.1.8 Carrier Freeze-out

At and above room temperature, essentially all the impurity atoms are thermally ionized and the concentration of mobile carriers is equal to the dopant concentration. As temperature decreases, the Fermi level approaches the valence band causing the mobile carriers to begin to freeze-out on the impurities and a corresponding decrease in electrical conductivity is observed [11]. The carrier freeze-out situation at the semiconductor surface under the gate is different than that in the bulk due to band bending [11]. The electric field of the channel interface depletion region sweeps out any mobile carriers and maintains complete ionization even at low temperatures. Approaching LNT carriers in the bulk begin to freeze-out, but there is essentially no effect on the ionized impurity concentration in the depletion region [11]. At strong freeze-out conditions of temperature below 30K, kink effect and transient phenomenon on I-V characteristics are observed.

Kink effect: At LT when impurity freeze-out occurs, the MOS devices in

saturation region experience kink effect that is attributed to self-polarization of the substrate due to the flow of majority carriers from body to source. The impurity freeze-out in the bulk leads to a strong increase of the back resistance which prevents the collection of drain impact ionization current through the body contacts. This results in a self biasing of the body and the source-body junction becomes forward biased. This causes a change in the threshold voltage and produces leveling of the drain current in saturation resulting in a kink in the I-V characteristics [9].

Transient effects: At LT operation when freeze-out occurs, when the gate voltage is increased from accumulation to inversion mode of operation, the drain current rises very rapidly to a value larger than the steady state value and then relaxes to the equilibrium steady state value. This is attributed to the slow formation of the depletion region that is dependent on temperature [17]. As soon as the gate voltage is stepped up, the space charge induced is mostly inversion charge since the dopant atoms have not had the time to emit charge and get ionized. However as time progresses, the dopant atoms get ionized and depletion region forms. As depletion region grows to its equilibrium level, the inversion charge decays to its steady state value. Since I_D is proportional to inversion charge, I_D exhibits the same type of transient behavior [17].

2.2.1.9 Leakage Current

With increasing operating temperature, there is an exponential increase in the leakage currents flowing across reverse-biased $p-n$ junctions such as the drain/source and substrate junctions in a MOSFET. These drain leakage currents are amplified by parasitic bipolar transistors which also cause latch-up. This amplification results in leakage currents that are much higher than the original diffusion leakage currents caused by the $p-n$ junction of the drain-substrate bulk diode [20]. At 250 °C, the leakage current increases by a factor of 4 than at 25 °C and becomes comparable to the drain current of the device [19]. These large leakage currents cause drifts in the operating points of the devices and the circuit and may also result in latch-up. Thus, circuit operation at high temperatures is affected by leakage currents and proper design is required to compensate for the leakage currents.

2.2.2 Effect on Op amp circuits

Following the study of temperature effects on MOSFETs, a brief discussion on the temperature dependence of op amp parameters is presented here using a simple two-stage CMOS op amp shown in Figure 2.2. The dependence of V_{TH} and μ on temperature has a major impact on the performance of the op amp.

The dynamic range of the op amp, which is impacted by offset voltage, noise and ICMR, is affected by variation in temperature. The change in threshold voltage causes bias point shifts and may thereby change the systematic offset voltage of the circuit. The noise contributed by the op amp also varies with a positive temperature coefficient. The input common-mode range (ICMR) is the input voltage range that is available for linear operation and is given by $V_{ICMR,max} - V_{ICMR,min}$, where

$$\begin{aligned} V_{ICMR,max} &= V_{DD} - |V_{DS,satM1}| - |V_{GS,M2,3}| \\ V_{ICMR,min} &= V_{SS} + V_{GS,M4} + V_{TH,M2} \end{aligned} \quad (2.7)$$

The temperature dependence of the threshold voltage affects the ICMR. At LT, the increase in threshold voltage lowers the ICMR. In order to increase the available ICMR, the $V_{DS,sat}$ of the device could be maintained at a minimum level of about 100mV for moderate inversion saturation operation. For strong inversion saturation, $V_{DS,sat}$ is

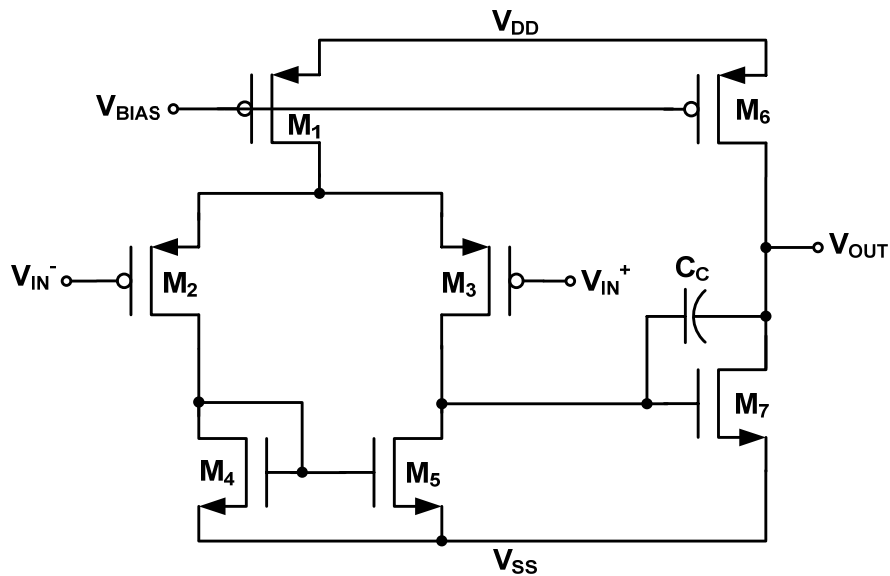


Figure 2.2 - Simple two-stage CMOS op amp

described by

$$V_{DS,sat} = \sqrt{\frac{2I_D}{\beta}} \quad (2.8)$$

$V_{DS,sat}$ can be lowered by reducing current I_D , increasing width, and by decreasing length. Any change in these device parameters would in turn affect the performance. For instance, reducing I_D would reduce the cut-off frequency of the op amp. With decreasing lengths, the cut-off frequency increases due to a reduction in the gate capacitance, but the offset voltage and flicker noise increase. Also, decreasing L reduces the output impedance and thus the gain decreases. As width is increased, the bandwidth decreases because of the increase in the drain/source capacitance [24]. So, there already exist many tradeoffs in designing an op amp for a specific temperature and extending the operability to extreme temperatures only adds more constraints to the design.

Considering the effect of mobility variations across temperature, the transconductance also changes with a negative temperature coefficient. This leads to a change in the gain A_{OL} , bandwidth and phase margin across temperature. When operated at HT, g_m decreases and so gain falls along with the bandwidth. To circumvent this problem, the current reference that is used to provide the bias current for the op amp could be designed to enhance robustness of the circuit across temperature. One method is to provide a constant- g_m bias circuit which stabilizes the small-signal performance. Providing a constant- g_m does not imply a constant current and thus results in changes in the large-signal response, such as the slew rate, across temperature. Another method is to provide a constant current across temperature. This constant current minimizes the variation of large-signal performance of the circuit, but at the expense of small-signal performance.

Therefore, proper design procedure is required to minimize the parameter variations across temperature. The following chapter deals with the design procedure used to build a robust circuit that operates well across temperature.

Chapter 3 Design of the Wide Temperature Range General-Purpose Op Amp

This chapter presents a detailed discussion on the design and implementation of the wide temperature general-purpose op amp. It begins with an analysis of the different stages used in the op amp's architecture. Then, the complete schematic is presented and the performance parameters of the op amp are derived. The next section presents the simulation results that are verified with the hand calculated values. The last section of this chapter presents the layout and implementation of the design.

3.1 Op amp Architecture

The design of an op amp is an iterative process which involves determining an appropriate architecture, designing the device sizes followed by analysis and simulation of the circuit to ensure that all specifications are satisfied. The specifications listed in Table 1.1 are examined in detail to determine the architecture. Although a specific value of open-loop gain is not included in the requirements, it is necessary to design the op amp with a high gain. This is done in order to ensure good closed-loop gain accuracy. Therefore, a two-stage architecture is employed for this op amp.

3.1.1 Input Stage

Generally, the choice of architecture for input stage is dictated by the requirements set by noise, input common-mode range and gain. With this design being targeted to be operable across a wide temperature range, it is desirable to use an architecture that is simple enough to meet the specifications and is not constrained too much by temperature variation. Some topologies that could be used for the input stage include simple differential stage, differential-cascode and folded-cascode. From these choices available, the topology that is most favorable to meet the specifications is employed for the design.

While cascoding in the differential input stage increases the output impedance and

thus helps in achieving higher gain, there is a reduction in the input common-mode range because of the extra voltage required by the cascode devices. Thus achieving a ground-sensing ICMR would not be possible with a differential-cascode input stage. In the folded-cascode topology, the direction of the signal from the input to the output devices is reversed and this offers good ICMR and wide output swing. By virtue of cascoding, high gain and good PSRR is also realized in this topology [5, 25, 26]. The drawback of using this topology is that the addition of devices for folding increases the noise of the circuit. Also, the load pairs carry more quiescent current. Further, at low temperature operation where the threshold voltage of devices increase, the presence of cascode devices adds additional constraints to already low voltage headroom available for the devices. Therefore, a simple differential topology as shown in Figure 3.1 is utilized in the input stage of the op amp.

In order to meet the specification of ground-sensing ICMR, a PMOS-input differential pair is used. Using PMOS input devices also provides 2-5 times lower flicker noise when compared to NMOS pairs because the lower hole mobility reduces the number of carriers being trapped in surface states [25, 27]. Also, careful sizing of the input pair with respect to the load devices is required to lower the circuit's thermal noise. The noise component of the load devices is scaled by the ratio of their transconductance to that of the input pair devices [26]. So, the g_m of the input differential pair needs to be larger than that of the load pair in order to ensure low input referred noise. The common-

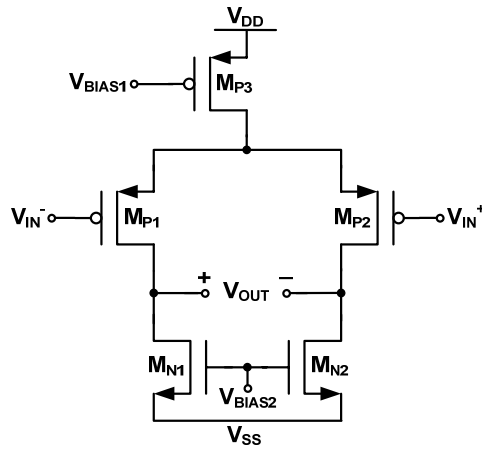


Figure 3.1 - Input stage of the op amp

mode (CM) output voltage of this differential-output input stage is not well-defined and is sensitive to mismatch and component variations [5, 25]. In order to maximize the output swing, this CM voltage needs to be stabilized at the mid-point between the signal swings. This is achieved by using a common-mode feedback (CMFB) loop that sets the CM level to a fixed reference voltage by means of a negative feedback. A detailed analysis of the CMFB circuit is presented in Section 3.2.7.

3.1.2 Output Stage

The important criteria for designing an output stage are good current driving capability, low power dissipation, the ability to provide voltage gain and good stability by avoiding additional parasitic poles [28]. The output stage used in this op amp is based on the circuit reported in [28] and is shown in Figure 3.2 along with its biasing section and a representation of the input stage. This circuit topology is simple and provides capability for rail-to-rail output swing, good current drive and low power dissipation while using relatively small sized transistors.

As shown in Figure 3.2, the output stage devices are biased using the output voltage from the input stage. The CMFB circuit stabilizes this voltage by setting it to a fixed reference value of V_{REF} , i.e. $V_{N2} = V_{N3} = V_{REF}$. Thus,

$$V_{GS,MN4} = V_{DS,MN4} = V_{GS,MN5} = V_{GS,MN8} \quad (3.1)$$

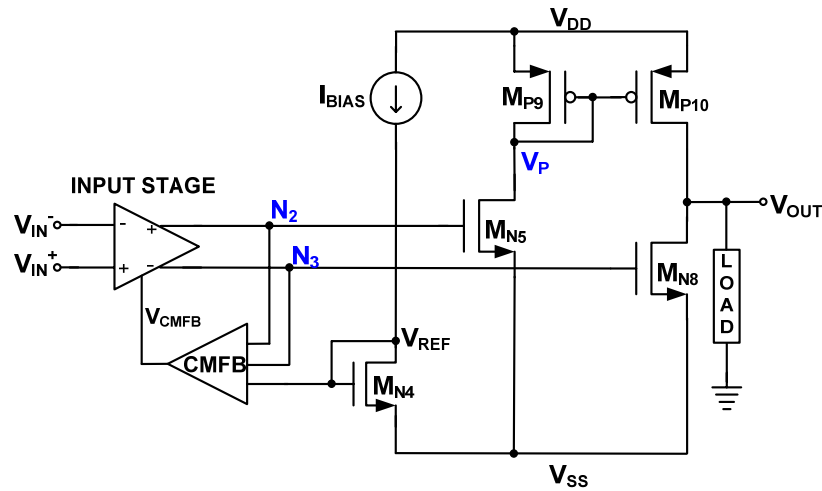


Figure 3.2 - The output stage along with input stage and CMFB block diagram [28]

Assuming that $(W/L)_{MP10}/(W/L)_{MP9} = (W/L)_{MN8}/(W/L)_{MN5}$ and also that the NMOS devices of M_{N4} , M_{N5} and M_{N8} are well matched, then the NMOS threshold voltages are equal and their overdrive voltages would also be the same. Equating the overdrive voltages, we obtain

$$\frac{I_{MN4}}{\left(\frac{W}{L}\right)_{MN4}} = \frac{I_{MN8}}{\left(\frac{W}{L}\right)_{MN8}} = \frac{I_{MN5}}{\left(\frac{W}{L}\right)_{MN5}} \quad (3.2)$$

where

$$V_{OVERDRIVE} = V_{GS} - V_{TH} = \sqrt{\frac{2I_D}{\beta(W/L)}} \quad (3.3)$$

Thus the quiescent currents in the output stage are set by the current flowing in the biasing circuit [28].

3.1.2.1 Drive performance

The drive capability in most output stages is limited by the limited V_{GS} of the output devices. For this output stage, assuming that the input stage does not impose any limit, then for a maximum sinking current from the output load V_{N3} , which is equal to $V_{GS,MN8}$, can swing all the way to V_{DD} resulting in a rail-to-rail V_{GS} for M_{N8} . Similarly for sourcing current to the output load, the $V_{GS,MN5}$ can swing up to V_{DD} forcing it into linear region. This causes the drain voltage of M_{N5} , V_P , to decrease toward V_{SS} and thus drive the PMOS devices with rail-to-rail V_{SG} voltages [28]. An equation for the maximum value of V_{SG} of M_{P10} can be derived by equating the currents flowing in M_{P9} and M_{N5} . Assuming $V_{GS,MN5} = V_{DD}$, using the first-order I-V equations for saturation and linear regions,

$$I_{D,MP9} = \frac{\beta_{MP9}}{2} (V_{SG,MP9} - |V_{THP}|)^2 = I_{D,MN5} = \beta_{MN5} \left[(V_{DD} - V_{THN}) V_{DS,MN5} - \frac{V_{DS,MN5}^2}{2} \right] \quad (3.4)$$

where β is the transconductance and V_{TH} is the threshold voltage. Using $\alpha = 2(\beta_{MN5}/\beta_{MP9})$, the above equation can be written as,

$$\left(V_{SG,MP9} - |V_{THP}|\right)^2 = \alpha V_{DS,MN5} \left[V_{DD} - V_{THN} - \frac{V_{DS,MN5}}{2} \right] \quad (3.5)$$

$$V_{SG,MP9} - |V_{THP}| = \alpha V_{DS,MN5} \frac{\left[V_{DD} - V_{THN} - \frac{V_{DS,MN5}}{2} \right]}{\left[V_{SG,MP9} - |V_{THP}| \right]} \quad (3.6)$$

using $V_{SG,MP9} = V_{DD} - V_{DS,MN5}$ we obtain,

$$V_{SG,MP9} - |V_{THP}| = \alpha V_{DS,MN5} \frac{\left[V_{DD} - V_{THN} - \frac{V_{DS,MN5}}{2} \right]}{\left[V_{DD} - V_{DS,MN5} - |V_{THP}| \right]} \quad (3.7)$$

For the $V_{SG,MP10, \max}$ condition, the value of $V_{DS,MN5}$ is very small, and so approximating,

$$V_{DD} - V_{THN} - \frac{V_{DS,MN5}}{2} \approx V_{DD} - V_{THP} - V_{DS,MN5} \quad (3.8)$$

we obtain,

$$V_{SG,MP9} - |V_{THP}| = \alpha V_{DS,MN5} = \alpha (V_{DD} - V_{SG,MP9} - V_{SS}) \quad (3.9)$$

and thus,

$$V_{SG,MP9, \max} = V_{SG,MP10, \max} = \frac{\alpha (V_{DD} - V_{SS}) + |V_{THP}|}{\alpha + 1} \quad (3.10)$$

Therefore, by sizing the transistors such that α is large, results in $V_{SG,MP10, \max}$ approaching a rail-to-rail voltage. Again, since the output devices can have rail-to-rail V_{GS} voltages, for a given output current, the devices can have smaller sizes [28].

Since the differential output from the first stage is complementary in nature—when one of the outputs is close to V_{DD} , the other is close to V_{SS} . So when one of the output transistors is heavily conducting, the other is OFF. Thus, the standby-power dissipation may be reduced. Furthermore, the output stage provides voltage gain and there is only one parasitic node in addition to the output node.

3.2 Complete Schematic

The complete schematic of the op amp is shown in Figure 3.3. The biasing circuit for the op amp is not included for brevity and will be discussed separately in Section 3.2.9. The input stage consists of the differential pair, M_{P1} - M_{P2} , loaded by current sinks,

M_{N1} - M_{N2} . The common-mode voltage at nodes N_2 and N_3 , the outputs of the input stage, is set by the common-mode feedback (CMFB) circuit comprising of M_{P4} , M_{P5} , M_{P6} , M_{P7} and M_{N3} . The reference voltage for the CMFB is provided by M_{P8} and M_{N4} . The output stage consists of transistors M_{N5} , M_{N8} , M_{P9} and M_{P10} . The biasing for the output stage is provided by the output from the input stage which is controlled by the CMFB circuit. As described in Section 3.1.2.1, the relative sizing of these output drivers determines the maximum V_{GS} swing available for driving. The aspect ratios of M_{N5} and M_{P9} are chosen to be equal and the value of α is 3.9 with a maximum possible $V_{SG,MP10}$ as 2.75 V. Also, in order to avoid excessive power dissipation in the output stage, the transistors M_{N5} and M_{P9} are sized to be half of that of M_{N8} and M_{P10} , respectively. With this output stage tailored for good load driving capability, the output swing of the op amp is expected to be nearly rail-to-rail. Frequency compensation is implemented using Miller capacitors C_1 , C_2 and their corresponding zero-nulling active resistors [29] M_{N6} and M_{N7} . The performance parameters of the op amp are analyzed in this section.

3.2.1 Open-loop Gain

An expression for the mid-band gain of the op amp can be derived by considering

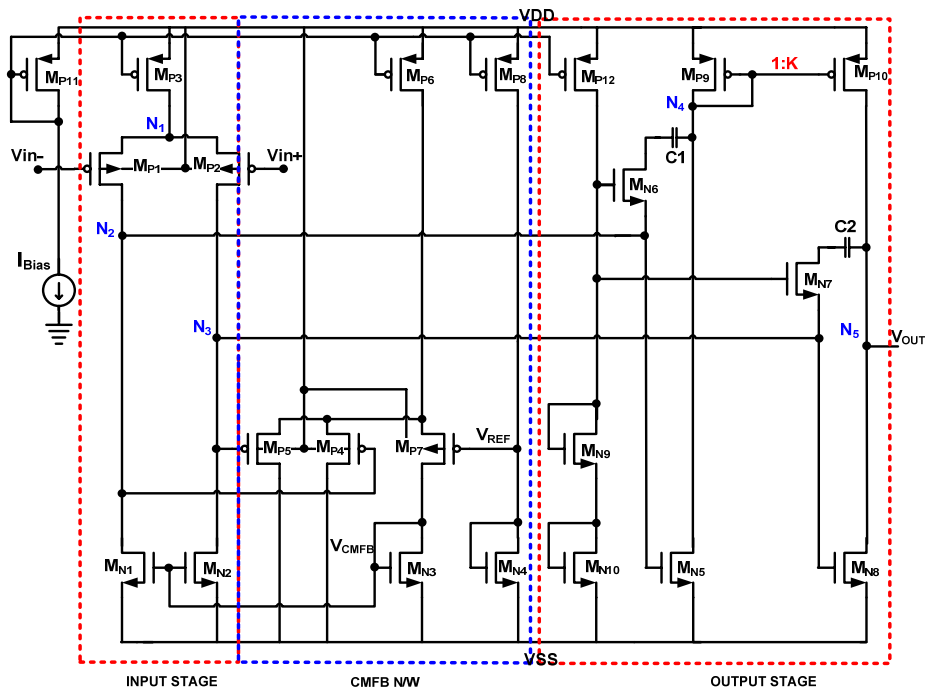


Figure 3.3 - Complete schematic of the op amp

the gain of the individual stages such as the input and output stages. The mid-band gain seen by the inputs to the differential input stage is symmetrical and can be expressed as

$$\begin{aligned} A_{V1} &= -\left(g_{m,MP1}\right)\left(r_{o,MP1} \parallel r_{o,MN1}\right) \\ A_{V1} &= -\left(g_{m,MP2}\right)\left(r_{o,MP2} \parallel r_{o,MN2}\right) \end{aligned} \quad (3.11)$$

The output stage has two gain paths from its input to the op amp's output. Assuming that the design follows equation (3.2), the gain offered by each path can be derived. For output stage shown in Figure 3.3, considering path 1 that is made up of transistors M_{N5} , M_{P9} and M_{P10} , the gain of M_{N5} and M_{P10} is given by equations (3.12) and (3.13) respectively and the total mid-band gain of that path is given by equation (3.15).

$$A_{V,MN5} = -\left(g_{m,MN5}\right)\left(r_{o,MN5} \parallel \frac{1}{g_{m,MP9}}\right) \approx -\frac{g_{m,MN5}}{g_{m,MP9}} \quad (3.12)$$

$$A_{V,MP10} = -\left(g_{m,MP10}\right)\left(r_{o,MP10} \parallel r_{o,MN8}\right) \quad (3.13)$$

$$A_{V2,path1} = A_{V,MN5}A_{V,MP10} = +\frac{g_{m,MN5}g_{m,MP10}}{g_{m,MP9}}\left(r_{o,MP10} \parallel r_{o,MN8}\right) \quad (3.14)$$

using $K = 2$, then $g_{m,MP10} = 2g_{m,MP9}$ and $g_{m,MN8} = 2g_{m,MN5}$,

$$A_{V2,path1} = +g_{m,MN8}\left(r_{o,MP10} \parallel r_{o,MN8}\right) \quad (3.15)$$

The second path has transistor M_{N8} providing the gain which can be expressed as

$$A_{V2,path2} = -g_{m,MN8}\left(r_{o,MP10} \parallel r_{o,MN8}\right) \quad (3.16)$$

Thus, the open-loop mid-band gain offered by the op amp is equal in magnitude for both the differential inputs and the overall gain is given as

$$\left|A_{V,total}\right| = \left|A_{V1}A_{V2}\right| = g_{m,MP1,2}g_{m,MN8}\left(r_{o,MP1,MP2} \parallel r_{o,MN1,MN2}\right)\left(r_{o,MP10} \parallel r_{o,MN8}\right) \quad (3.17)$$

Using appropriate values, as shown in Appendix, A.1, for g_m and r_o , the open-loop gain of the op amp is calculated to be 93 dB.

3.2.2 Frequency Compensation

In Figure 3.3, the op amp has bandwidth-limiting poles at nodes N_2 , N_3 and N_5 . Frequency compensation is provided using two pole-splitting Miller capacitors and their corresponding zero-nulling MOS active resistors. The location of the dominant pole is

determined by the nodes N_2 and N_3 . The value of the compensation capacitors is found using the requirement for frequency stability, as in [29]

$$C_C \geq \sqrt{\frac{g_{m,MN5,MN8}}{g_{m,MP1,MP2}}} C_{N2,N3} C_L \quad (3.18)$$

where $g_{m,MN5,MN8}$ and $g_{m,MP1,MP2}$ are the transconductances of the output drivers and the input differential pairs respectively, $C_{N2,N3}$ is the respective node capacitance at nodes N_2 and N_3 and C_L is the load capacitance. The value of the zero-nulling resistor needs to be maintained across any variation in process, temperature and supply voltage (PTS) in order to ensure that the pole-zero doublet does not adversely impact the settling time of the op amp [26, 41]. The temperature tracking compensation [26] implemented here enables effective biasing of each active resistor across any variation in PTS. The biasing for the MOS resistors is realized using diode-connected MOSFETs (M_{N9} - M_{N10}), current source (M_{P12}) and the input to second stage. The value of the active resistors, M_{N6} , M_{N7} is made to track the g_m of M_{N5} and M_{N8} respectively. This is achieved through device sizing and careful matching of M_{N9} , M_{N10} with M_{N6}/M_{N7} and M_{N5}/M_{N8} respectively. The sizing of M_{N6} , M_{N7} and thus the value of each active resistor is determined by the condition for pole-zero cancellation [26] which is

$$\left(\frac{W}{L}\right)_{MN6,MN7} = \sqrt{\left(\frac{W}{L}\right)_{MN9} \left(\frac{W}{L}\right)_{MN5,MN8} \frac{I_{D,MN5,MN8}}{I_{D,MN9}}} \left[\frac{C_C}{C_C + C_L} \right] \quad (3.19)$$

The pole-zero cancellation condition is a function of device sizes and the relative values of bias currents and capacitors that can be controlled by proper matching. Hence the value of the active resistor is totally independent of variations in process, temperature and supply voltage. Furthermore, this technique allows the use of small value compensation capacitors of about 6 pF for up to 100 pF load condition.

The location of the dominant pole for the compensated op amp can be derived from the time constants of nodes of N_2 and N_3 , and is given by [28]

$$p_D = -\frac{1}{r_0(C_{M1} + C_{M2})} \text{ rad/s} \quad (3.20)$$

where r_0 is the output impedance of the input stage, $C_{M1} = \left(1 + \frac{g_{m,MN5}}{g_{m,MP9}}\right) \frac{C_1}{2}$ is half of the Miller capacitance associated with compensation capacitor C_1 at node N2 and $C_{M2} = g_{m,MN8} R_L C_2$ is the Miller capacitance due to C_2 at node N3. The second pole is at the output node N5 and is given by

$$p_2 = -\frac{g_{m,MN8}}{C_L} \text{ rad/s} \quad (3.21)$$

The frequency at which the gain is unity is given by the unity-gain bandwidth (UGBW) which can be approximated as

$$UGBW = \frac{g_{m,MP1,MP2}}{2\pi(C_1 + C_2)} \text{ Hz} \quad (3.22)$$

Using appropriate values for g_m , C_1 and C_2 , the calculated $UGBW$ is 2.35 MHz.

3.2.3 Input common mode range

The PMOS differential input pairs provide the feasibility to extend the lower ICMR to V_{SS} . Connecting the substrates of the input devices to V_{DD} improves the ICMR by increasing the threshold of the PMOS devices due to body effect. The minimum value of the input common mode range is given by

$$\begin{aligned} V_{ICMR,\min} &= V_{SS} + V_{SG,MP1} - V_{DSsat,MP1} + V_{GS,MN3} \\ &= V_{SS} + V_{SG,MP1} - \left(V_{SG,MP1} + |V_{TH,MP1}|\right) + V_{GS,MN3} \\ &= V_{SS} - |V_{TH,MP1}| + V_{GS,MN3} \end{aligned} \quad (3.23)$$

From (3.23) it is evident that an increase in $|V_{THP}|$ of the PMOS devices improves the lower limit of ICMR and the value can in fact extend below V_{SS} .

The maximum limit of ICMR is determined by the V_{SG} of the input pair and the overdrive of the current source. It can be expressed as

$$\begin{aligned} V_{ICMR,\max} &= V_{DD} - V_{SG,MP1} - V_{SDsat,MP3} \\ V_{ICMR,\max} &= V_{DD} - \left(V_{SDsat,MP1} + |V_{THP,MP1}|\right) - V_{SDsat,MP3} \end{aligned} \quad (3.24)$$

For 3.3-V V_{DD} , $V_{ICMR,\max}$ should exceed mid-supply.

3.2.4 Noise

The input stage determines the noise of the op amp. As discussed in section 3.1.1, choosing PMOS as input devices lowers flicker noise. Also, the noise component of the load devices is scaled by the ratio of their transconductance to that of the input pair devices. So the transconductance of the input differential pair needs to be larger than that of the load pair in order to ensure low input referred noise. There exists a trade-off between noise and the output swing of the stage. Generally, the overdrive voltage of the current loads is minimized to realize a wide output swing, but for a fixed current bias this increases the transconductance (due to increased W) and thereby results in a larger input referred noise.

A quick estimate on the equivalent input noise of the op amp can be performed by considering the noise of the input stage. The noise contributed by the subsequent stages is reduced by the gain of the differential-input stage when referred to the input, so these noise stages can be neglected for the hand analysis. Referring to Figure 3.3, considerable noise is contributed by the input devices of M_{P1} , M_{P2} and the current loads M_{N1} and M_{N2} while the tail current source's noise is neglected in the differential mode analysis. The total thermal and flicker noises of the devices is referred to the input to obtain the equivalent input noise as [25, 26]

$$\overline{V_{n,in}^2} = 8kT \left(\frac{2}{3g_{m,MP1}} + \frac{2g_{m,MN1}}{3g_{m,MP1}^2} \right) + \frac{2}{f} \left(\frac{K_N}{C_{OX}W_N L_N} \frac{g_{m,MN1}^2}{g_{m,MP1}^2} + \frac{K_P}{C_{OX}W_P L_P} \right) \quad (3.25)$$

where k is the Boltzmann constant, T is absolute temperature, $g_{m,MP1}$ and $g_{m,MN1}$ are the transconductances of the transistors M_{P1} and M_{N1} respectively, K_N and K_P are the process-dependent flicker noise coefficients of NMOS and PMOS devices and W , L are the dimensions of M_{N1} and M_{P1} . The g_m values at quiescent operating point for these devices were used for the hand calculation of op amp noise. The flicker noise coefficients were derived from the $1/f$ noise corner frequency obtained by simulating CMOS devices configured as simple common-source amplifiers. The setup is discussed in Appendix A.2. From the calculations, the input-referred thermal noise of the input stage is 19 nV/ $\sqrt{\text{Hz}}$ and the flicker noise at 100 KHz is 64.5 nV/ $\sqrt{\text{Hz}}$, thus the total input noise of the op amp

at 100 KHz is estimated to be 67.2 nV/ $\sqrt{\text{Hz}}$ which is below the specified noise limit of 100 nV/ $\sqrt{\text{Hz}}$.

3.2.5 Offset Voltage

The good symmetry of the op amp's topology is expected to provide a low offset voltage. An approximate analysis to characterize the systematic and random input-referred offsets of the op amp can be performed by considering the offsets introduced by the input stage and ignoring those of the output stage. Similar to the noise analysis, an expression for the offset voltage can be derived and referenced to the input as input offset voltage. Random offsets arise due to the presence of mismatches in supposedly identical pairs of devices, such as the input pair M_{P1} and M_{P2} and the load pair M_{N1} and M_{N2} . The mismatch in devices parameters μ , C_{OX} , W , L and V_{TH} cause I_D mismatch for a given V_{GS} or V_{GS} mismatches for a given I_D [30].

For the input stage of Figure 3.3, the random offset introduced by the input transistor pair can be expressed as [5, 26]

$$V_{OS,P} = \frac{(V_{SG} - |V_{TH}|)_P}{2} \left[\frac{\Delta(W/L)}{W/L} \right]_P + \Delta V_{TH,P} \quad (3.26)$$

where the first term represents the effects of W/L mismatch and can be minimized by reducing the overdrive voltage $V_{OV,P} = (V_{SG} - |V_{TH}|)_P$. The second term is for the threshold mismatch of the input transistors. Similarly, an expression for the offset due to the load pair is given by (3.27) [5, 26] and that for total input referred random offset is given in (3.28) as the sum of the offsets.

$$V_{OS,N} = \frac{(V_{GS} - V_{TH})_N}{2} \left[\frac{\Delta(W/L)}{W/L} \right]_N + \Delta V_{TH,N} \quad (3.27)$$

$$\begin{aligned}
V_{OS,in} = & \frac{|V_{GS} - V_{TH}|_P}{2} \left[\frac{\Delta(W/L)}{W/L} \right]_P + \Delta V_{TH,P} \\
& + \left[\frac{(V_{GS} - V_{TH})_N}{2} \left[\frac{\Delta(W/L)}{W/L} \right]_N + \Delta V_{TH,N} \right] \frac{g_{mN}}{g_{mP}}
\end{aligned} \tag{3.28}$$

These equations suggest that, in order to minimize the random offset, the overdrive voltages need to be reduced and the aspect ratio of the load pair needs to be chosen such that the g_m of the load pair is smaller than that of the input devices. Meeting the latter also helps in reducing the input referred noise. Also, careful layout techniques, such as common centroid layout techniques, ensure proper matching between the transistors and reduce the random offset.

Systematic offset arises due to the design of the circuit and may be present even when all the devices are perfectly matched. A major source of systematic offset is the effect of channel length modulation on the accuracy of current mirror devices when the drain voltages are not equal. Systematic offset is examined by applying a mid-supply voltage to the op amp's input and determining the deviation of output voltage from the ideal mid-supply value. In the op amp of Figure 3.3, the output of the first stage supplies the gate-source bias for the output stage. Ideally, for zero offset, this bias voltage should be such that it sets the output of the op amp at mid-supply but there is usually a deviation from the desired value and an offset exists [5].

The CMFB network helps in the reduction of systematic offset by ensuring that the output voltages of the input stage (V_{N2}, V_{N3}) are equal to the required quiescent input voltages of the second stage. The CMFB sets the dc output voltages of V_{N2}, V_{N3} to be equal to the gate-source voltage, V_{REF} , of the device M_{N4} , from which quiescent currents are mirrored to the second stage. By fixing V_{N2}, V_{N3} to be equal to a constant V_{REF} , the dc common mode output of first stage is made independent of the dc input voltage. Thus when the second stage is supplied with the same quiescent dc voltage as M_{N4} , the devices are well matched and the currents in the output devices of M_{P10} and M_{N8} can ideally be equal and provide a zero offset voltage referred to the input. By choosing an appropriate value of gate length L , channel length modulation effects can be minimized.

For the input stage in Figure 3.3, the devices M_{N1} , M_{N2} and M_{N3} need to be matched and the output voltages of V_{N2} and V_{N3} also need to be equal. With the same V_{GS} and V_{TH} voltages for M_{N1} - M_{N2} and M_{P1} - M_{P2} pairs respectively, the overdrive voltages are also equal. So, $V_{OV,MN1} = V_{OV,MN2} = V_{OV,MN3}$, where $V_{OV} = \sqrt{\frac{2I_D}{\mu C_{OX} (W/L)}}$ and thus

$$\frac{I_{D,MN1}}{(W/L)_{MN1}} = \frac{I_{D,MN2}}{(W/L)_{MN2}} = \frac{I_{D,MN3}}{(W/L)_{MN3}} \quad (3.29)$$

With the aspect ratios chosen to satisfy the equation (3.29) and using identical values for the lengths and the widths, the current densities are equal and can result in an operating point that is insensitive to process variations [5]. Similarly, for the second stage, the condition for good matching can be expressed as

$$\frac{I_{D,MN4}}{(W/L)_{MN4}} = \frac{I_{D,MN5}}{(W/L)_{MN5}} = \frac{I_{D,MN8}}{(W/L)_{MN8}} \quad (3.30)$$

3.2.6 Output Swing

One interpretation of output swing is the range of output voltages over which all the transistors operate in saturation region thus maintaining the op amp's overall gain. For the op amp, M_{N8} leaves saturation if the output voltage is lower than $V_{OV,MN8} - V_{SS}$. Similarly, the transistor M_{P10} enters triode region when output increases above $V_{DD} - |V_{OV,MP10}|$. Therefore, the output swing for maximum op amp gain is

$$V_{OV,MN8} - V_{SS} \leq V_{OUT} \leq V_{DD} - |V_{OV,MP10}| \quad (3.31)$$

This shows that if the overdrive voltages are chosen to be less than 0.2 V for the output devices, then the output swing meets the required specification of within 0.2 V of each supply.

3.2.7 Slew Rate

The Slew Rate of the op amp can be represented as [26],

$$SR = \frac{I_{tail}}{C_C} \quad (3.32)$$

where I_{tail} is the total current supplied to the input differential pair and C_C is the value of the compensation capacitor. The calculated slew rate is approximately 7 V/ μ s.

3.2.8 Common-mode Feedback (CMFB)

As discussed in Section 3.1.1, the CMFB circuit is required to set a well-defined dc operating point for the differential-output of the input stage and thereby provides biasing to the output stage. The CMFB is a negative feedback network which works by sensing the outputs, comparing it with a reference voltage and returning an error signal to the amplifier's bias network [26]. In designing the CMFB, the following considerations are given importance [31, 32]. First, the ICMR of the CMFB should not restrict the maximal output swing of the op amp. The bandwidth of the CMFB needs to be greater than that of the differential input stage. Also, the CMFB amplifier should provide high common-mode gain, comparable to that of the differential-mode gain.

Different topologies for realizing a CMFB are discussed in [33, 34]. A continuous-time CMFB topology is employed here and is shown, along with the input stage, in Figure 3.4. Z_1 and Z_2 represent the effective impedance added by the output stage's compensation network to these nodes. The output voltages are sensed by the differential pair, M_{P4} , M_{P5} . Depending on the voltage sensed with respect to V_{REF} , the current sourced from M_{P6} is divided among the transistors M_{P4} , M_{P5} and M_{P7} . The error current through M_{P7} and M_{N3} is converted to a voltage, V_{CMFB} . This voltage is used to regulate the gate bias of the current load transistors, M_{N1} and M_{N2} and thus fix the voltages at nodes N_2 and N_3 to V_{REF} . The reference voltage (V_{REF}) is generated from a diode-connected NMOS device, M_{N4} . The matching/balance between the voltage sensing transistors is very important in order to avoid any dependency of the V_{CMFB} on the differential output of the input stage. Furthermore, these transistors need to be matched with M_{P7} for accurate comparison with V_{REF} . Also, the current through the transistor M_{N3} sets the gate bias voltage for the input current loads and therefore matching between these NMOS transistors is essential. For proper matching, transistors M_{P4} , M_{P5} are sized to have

single-pole system within the bandwidth and therefore stability of the op amp is not compromised. The GBW of the loop can be expressed as [37]

$$GBW = A_{CMFB} p_D \approx \frac{g_{m,MN1}(r_{o,MN1} \parallel r_{o,MP1}) \frac{g_{m,MP4}}{g_{m,MN3}}}{2\pi(r_{o,MN1} \parallel r_{o,MP1})C_{M1}} \quad (3.34)$$

where the loop gain is from equation (3.33). Substituting values in (3.34) gives the expected bandwidth for the CMFB to be around 1 MHz. To verify this analysis, the transmission loop frequency response of the CMFB was simulated and the Bode plot of the magnitude and phase response is presented in Figure 3.5. The magnitude of the gain is 40 dB which agrees well with the calculated result. Also the dominant pole occurs around 5.8 KHz with a GBW of 900 KHz. The plots show the presence of a pole-zero doublet before the unity-gain bandwidth of the op amp. The location of this doublet is given in [43] as

$$p_1 = \frac{-g_{m,MP5}}{2\left(\frac{C_{M1}C_{M2}}{C_{M1} + C_{M2}}\right)} \text{ and } z_1 = \frac{-2g_{m,MP5}}{C_{M1} + C_{M2}} \quad (3.35)$$

where C_{M1} and C_{M2} are the Miller capacitances due to the compensation capacitors as in (3.20). If the pole and zero are placed within a decade, they cancel out each other and thus do not cause instability in the frequency-response or a large settling time in the transient response. Also, the phase plot shows that the CMFB has a phase margin of 90° .

In order to determine the ICMR of the CMFB circuit alone, a ramp voltage was applied as common-mode input to M_{P4} and M_{P5} . The range of voltages for which all the transistors in the CMFB (M_{P4} - M_{P8} , M_{N3} - M_{N4}) operate in saturation was obtained from simulations as -1.2 to -0.6 V for complementary power supplies (± 1.65 V). At dc, the V_{REF} is fixed as -0.915 V. With reasonable gain in the output stage of the op amp, for a maximum output swing the required voltage swing at the output nodes of the input stage is quite small. So the CMFB does not restrict the output swing. In order to verify the performance, transient simulations were performed with common-mode and differential signals applied to the op amp which is configured as a non-inverting, unity-gain buffer. The transient response of the CMFB circuit for a common mode input of 2.2 Vpp at 1

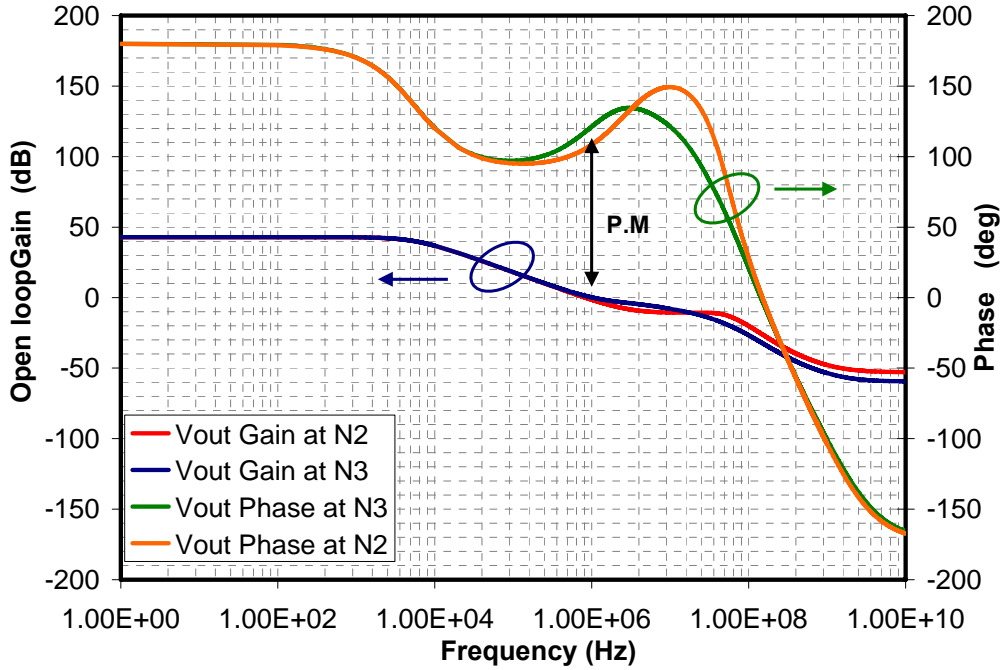


Figure 3.5 - Simulated frequency response of CMFB circuit

KHz to the op amp inputs is shown in Figure 3.6 (a). Input was restricted to 2.2 V_{pp} due to the ICMR constraints of the op amp. Figure 3.6 (b) presents the case of maximum output with differential inputs. Both plots show that the output swing of the op amp is not limited by CMFB and the nodes N₂ and N₃ are regulated throughout the swing with all the devices of CMFB circuit in saturation for the entire range of input voltages.

By fixing the dc quiescent output voltage of the input stage, the CMFB helps in reducing the op amp's offset and offset drift across temperature. For instance, consider the change in bias current with the change in temperature. The mobility and therefore the g_m also vary, but the rate of change is different in the NMOS and PMOS devices. Hence there would be a change in the random offset voltage given by (3.28). With the CMFB, the output voltage at node N₃ can be written as,

$$V_{O,N3} = -V_{SG,MP5} + V_{SD,MP7} + V_{GS,MN1} \quad (3.36)$$

$$V_{O,N3} = -\sqrt{\frac{2I_{D,MP5}}{\beta\left(\frac{W}{L}\right)_{MP5}}} - |V_{TH,MP5}| + V_{SD,MP7} + \sqrt{\frac{2I_{D,MN2}}{\beta\left(\frac{W}{L}\right)_{MN2}}} + V_{TH,MN2} \quad (3.37)$$

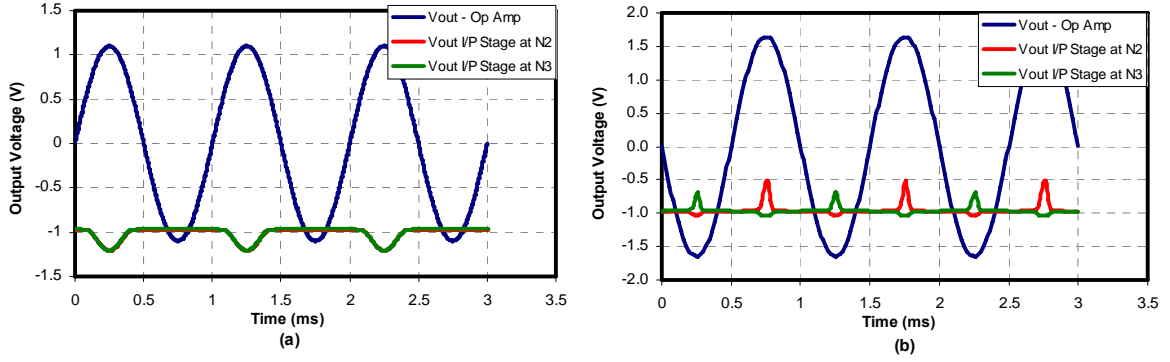


Figure 3.6 - CMFB transient response for (a) common-mode signal and (b) differential-mode signal

With the currents expressed in terms of the bias current I_{SS} of the input differential stage,

$$V_{O,N3} = -\sqrt{\frac{2(kI_{SS} - I_{D,MN3})/2}{\beta\left(\frac{W}{L}\right)_{MP5}}} - |V_{TH,MP5}| + V_{SD,MP7} + \sqrt{\frac{2(I_{SS})/2}{\beta\left(\frac{W}{L}\right)_{MN2}}} + V_{TH,MN2} \quad (3.38)$$

With equal currents in M_{P3} and M_{P6} , $k = 1$, and at quiescent point, $I_{D,MN3} = I_{D,MP6}/2 = I_{SS}/2$. Thus,

$$V_{O,N3} = -\sqrt{\frac{(I_{SS})/2}{\beta\left(\frac{W}{L}\right)_{MP5}}} - |V_{TH,MP5}| + V_{SD,MP7} + \sqrt{\frac{I_{SS}}{\beta\left(\frac{W}{L}\right)_{MN2}}} + V_{TH,MN2} \quad (3.39)$$

From equation (3.39) it can be inferred that the change in dc operating point due to a change in bias current I_{SS} can be minimized by sizing the M_{P4} and M_{P5} transistors relative to that of M_{N1} and M_{N2} . Doing this, for a change in bias current with temperature, the voltage variation in nodes N_2 and N_3 can be reduced or even cancelled. Furthermore, the CMFB action forces the V_{N2} and V_{N3} voltages to track V_{REF} across temperature. Thus the CMFB minimizes the offset voltage drift across temperature. Figure 3.7 presents the change in the node voltages of N_2 and N_3 and their difference for a change in the bias current from $1 \mu\text{A}$ to $100 \mu\text{A}$. The difference between the node voltages is $860 \mu\text{V}$ and so a very small drift in the offset voltage across temperature is expected using this CMFB circuit.

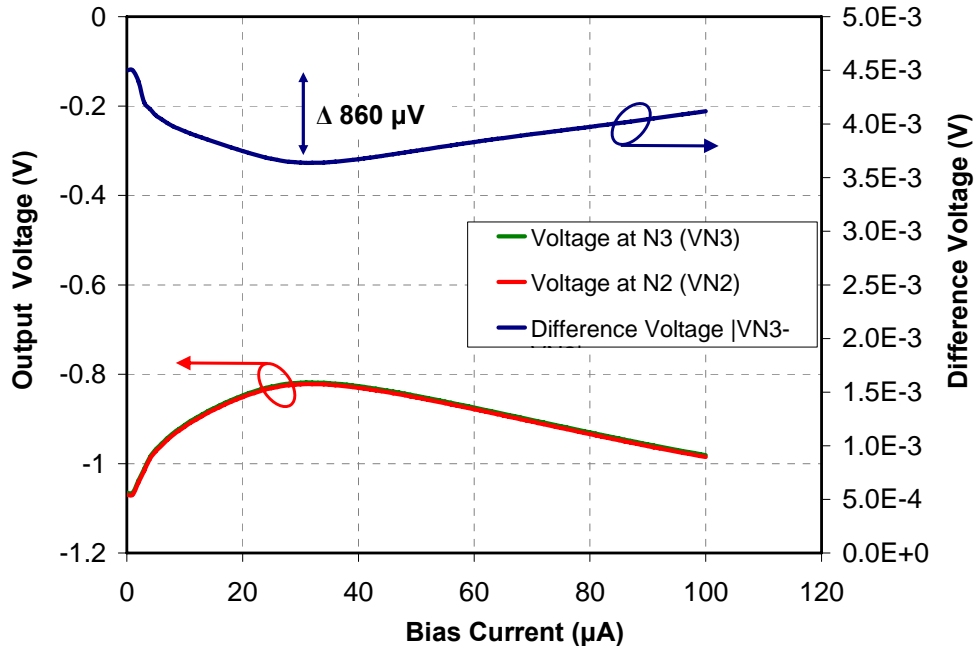


Figure 3.7 - Plot showing the difference voltage at output of input stage vs. bias current

3.2.9 Current Reference

The current reference circuit biases the op amp and plays an important role in the op amp's performance variations across temperature. The choice of the current reference circuit is driven by its capability to ensure minimum variation in small-signal as well as large-signal performance of the op amp. The use of a constant- g_m current reference [42] minimizes variations in small-signal performance, like bandwidth, but at the cost of large-signal performance, such as slew rate. While a constant current reference optimizes large-signal performance across temperature, small-signal performance is affected by significant changes. Therefore, in order to provide minimum variation in the overall performance across temperature, a constant inversion coefficient (IC) current reference that maintains a constant IC for MOSFETs across temperature has been used here [35]. The current has a temperature exponent of 0.5 to provide a tradeoff between constant- g_m and constant-current reference circuits.

The schematic of the current reference is shown in Figure 3.8. A startup circuit is required to ensure current generation on power-up and can be found in [35]. The circuit

has a PTAT generator that uses hetero-junction bipolar transistors (HBT) to generate a PTAT voltage (V_{PTAT}). PTAT structures are stacked to realize a higher V_{PTAT} for improved accuracy. This voltage is converted to current by the transconductor stage. The output current is also used to bias the PTAT generator. The transconductor's output current is also replicated and feedback as a tail current bias to the transconductor itself. In this manner, g_m/I_D regulation is achieved to provide constant IC. An output current of approximately 20 μA is provided. The output current is described by

$$I \propto 2\beta U_T^2 \quad (3.40)$$

where β is a product of PMOS mobility and U_T is the thermal voltage. The temperature exponent of β is -1.5 and thus a current of $+0.5$ temperature exponent is achieved. Further, the use of HBTs enhances the robustness of the circuit across a wide temperature range, especially at cryogenic temperatures.

3.3 Simulation Results

Simulations were performed using Spectre in order to verify and characterize the performance of the op amp across temperature. The circuits used for each characterization are identical to those used in testing and are discussed in-depth in Chapter 4. The results presented here are from simulations of the extracted layout, with a

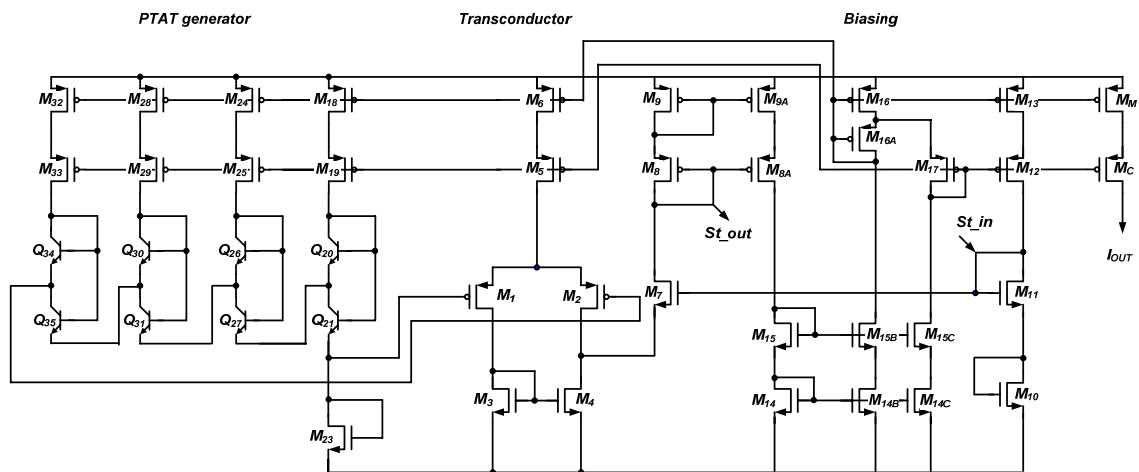


Figure 3.8 - Schematic of constant IC current reference circuit [35]

50 pF load, using the BSIM3v3 typical corner models for IBM 5AM process and with a supply voltage of 3.3 V.

Simulations for the offset voltage, without considering any mismatch between the transistors, resulted in a very low offset of 30 μV . Therefore, to get a realistic estimate, Monte Carlo simulations were performed with a $\pm 3\sigma$ variation in the threshold and process parameters. The magnitude of the average offset voltage over 100 samples was determined to be 1.3 mV at 25 $^{\circ}\text{C}$. Due to the unavailability of continuous models across the full temperature range of -180°C to 125 $^{\circ}\text{C}$, Monte Carlo simulations were run for -55°C to 125 $^{\circ}\text{C}$ and the offset variation was 12 μV across this range with a drift of 70 nV/ $^{\circ}\text{C}$.

Figure 3.9 presents the ICMR simulation plots across temperature. Here the op amp is in a unity-gain non-inverting configuration and $V_{\text{DD}}/V_{\text{SS}}$ is $\pm 1.65\text{ V}$. It can be seen that the op amp is ground sensing and the upper ICMR value decreases with fall in temperature. Figure 3.10 shows the open-loop gain and phase plot for the frequency compensated op amp. At 25 $^{\circ}\text{C}$, the A_{OL} is 89 dB with UGBW of 2.75 MHz and a phase margin of 74 $^{\circ}$. The response to small-signal transient inputs is presented in Figure 3.11 and Figure 3.12. The simulated rise time and fall time are 94 ns and 96 ns respectively, at 25 $^{\circ}\text{C}$. Figure 3.13 and Figure 3.14 show the large-signal response across temperature.

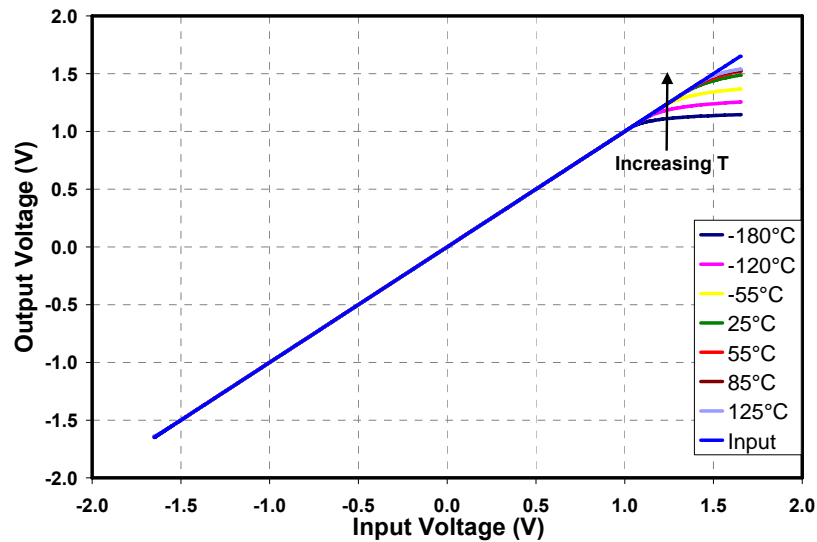


Figure 3.9 - Simulation result for ICMR across temperature

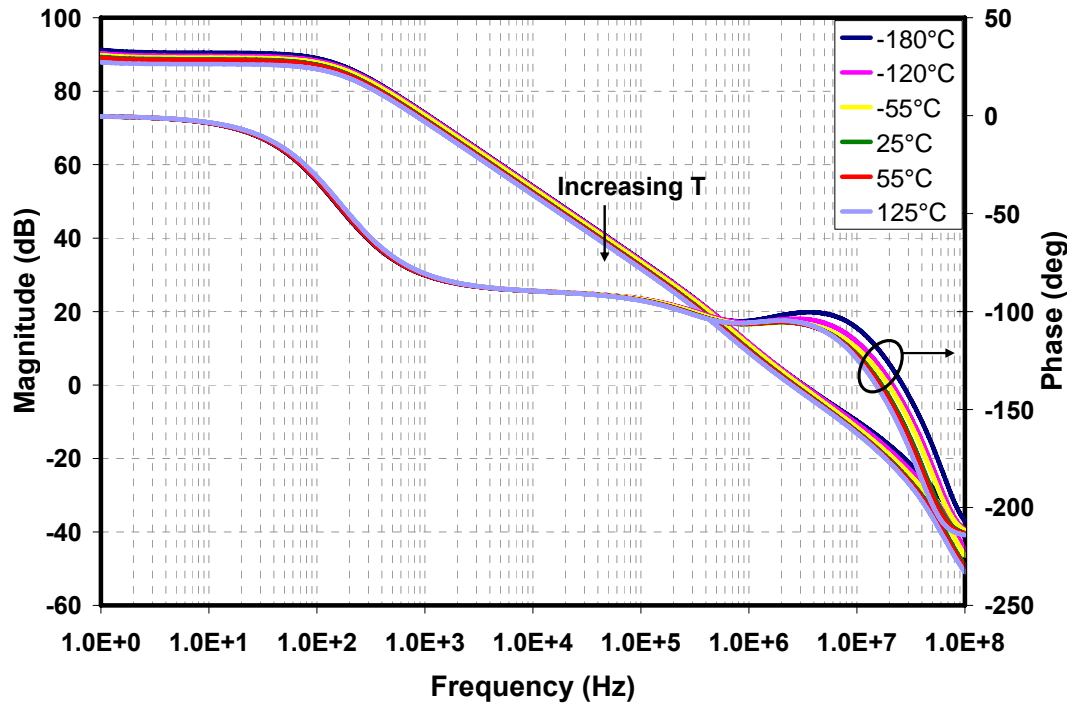


Figure 3.10 - Simulation result for open-loop gain and phase across temperature

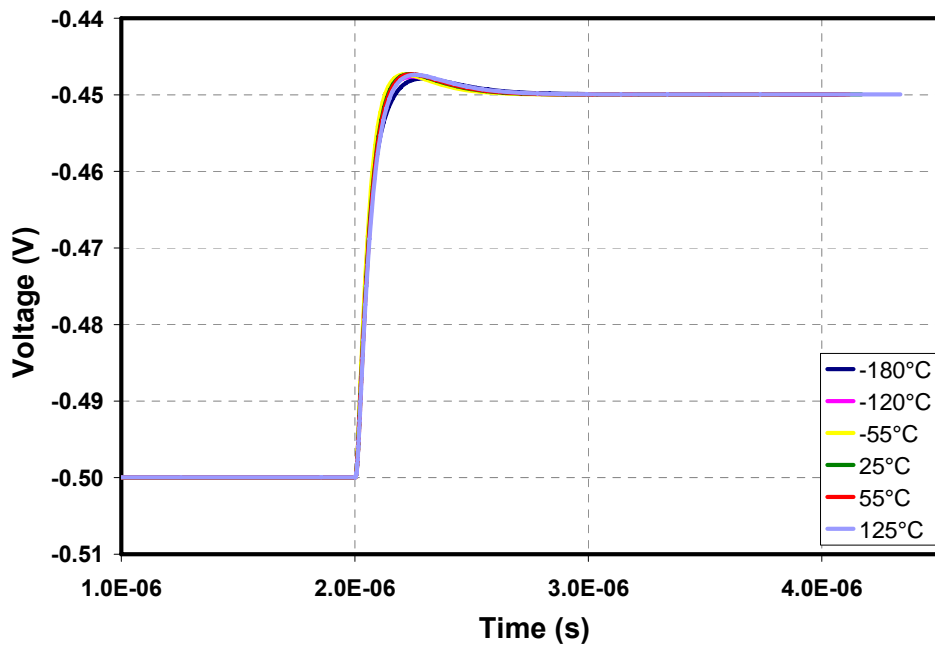


Figure 3.11 - Simulation result for small-signal rise time across temperature

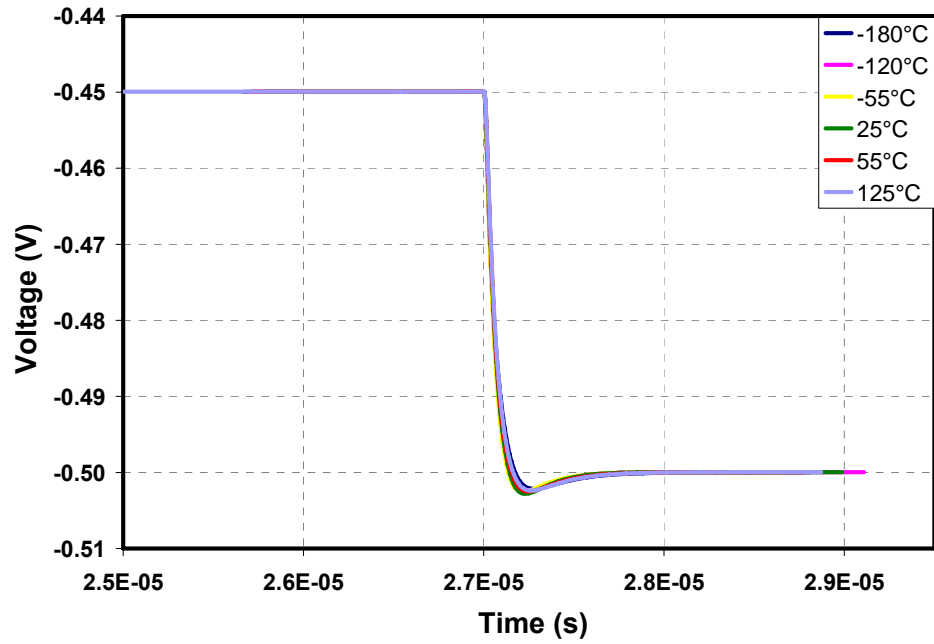


Figure 3.12 - Simulation result for small-signal fall time across temperature

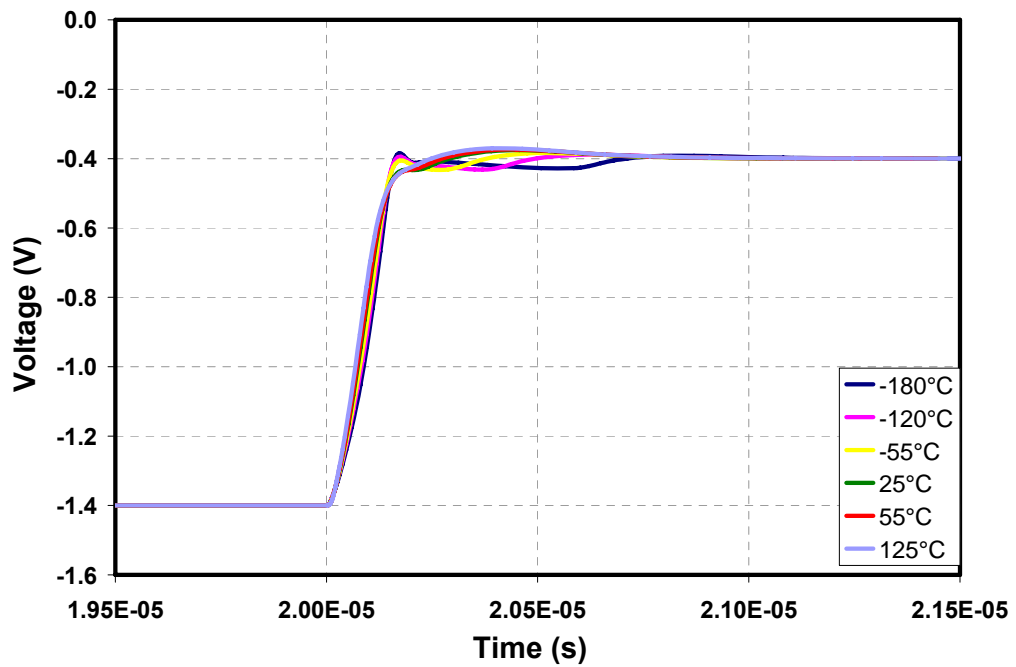


Figure 3.13 - Simulated positive slewing edge across temperature

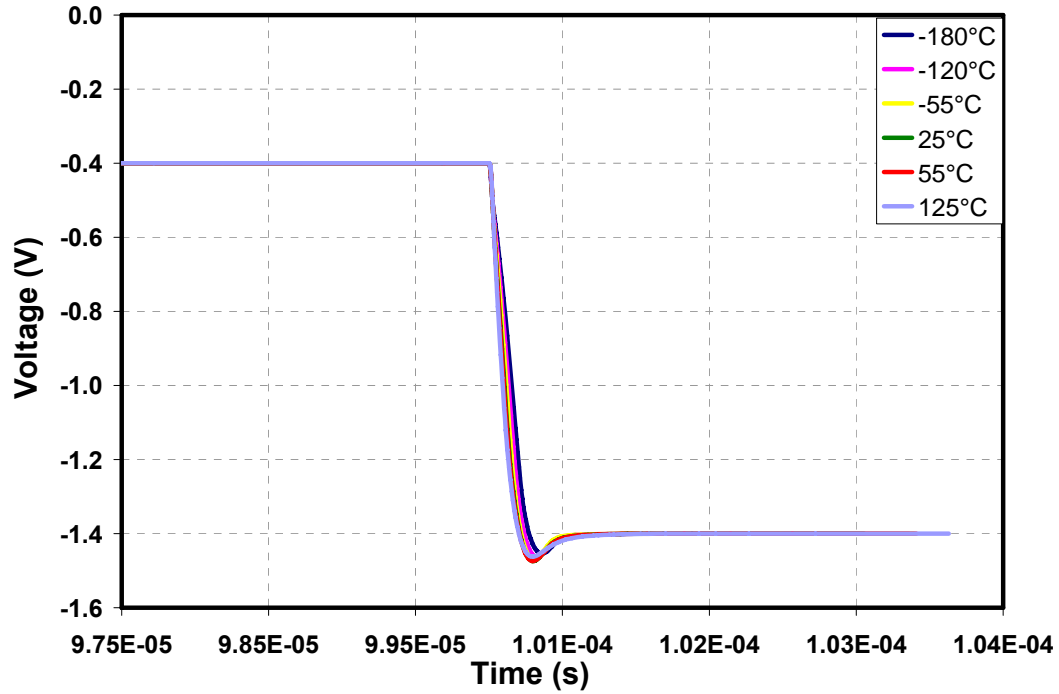


Figure 3.14 - Simulated negative slewing edge across temperature

The simulation result for the input referred noise voltage, e_{ni} , of the op amp is shown in Figure 3.15. At 25 °C, the simulated e_{ni} at 100 KHz is 66.7 nV/ $\sqrt{\text{Hz}}$ and it matches well with the hand calculated value of 67.2 nV/ $\sqrt{\text{Hz}}$. But it should be noted that these values are based on a pessimistic noise model [38] so the measured noise voltage is expected to be smaller.

Since the PSRR and CMRR depend on the change in the offset voltage induced by a change in power supply and common-mode voltage respectively, Monte Carlo simulations were performed to characterize PSRR and CMRR at dc and across temperature. Figure 3.16 and Figure 3.17 show the simulation results for PSRR and CMRR across temperature. Note that at -180 °C and -120 °C, the results are constant across the 100 samples due to the unavailability of continuous temperature models below -55 °C. At 25 °C, the simulated PSRR is 89 dB and the simulated CMRR is 67 dB.

Figure 3.18 presents the change in bias current generated by the constant IC current reference circuit across temperature. These simulation results will be compared with measured data in Chapter 4.

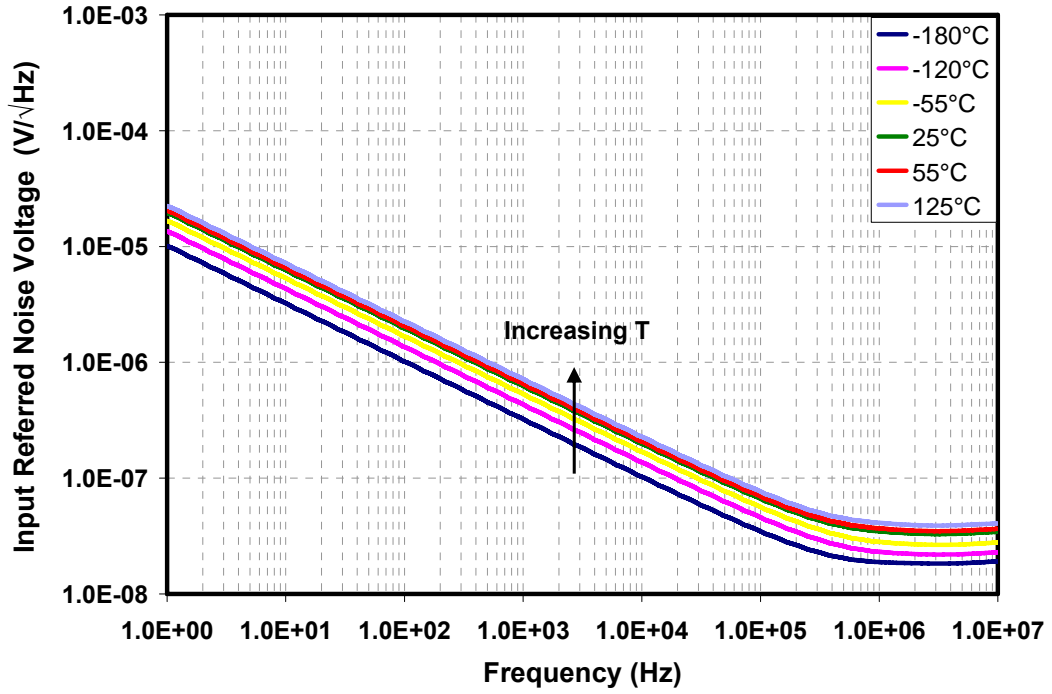


Figure 3.15 - Simulated input referred noise voltage across temperature

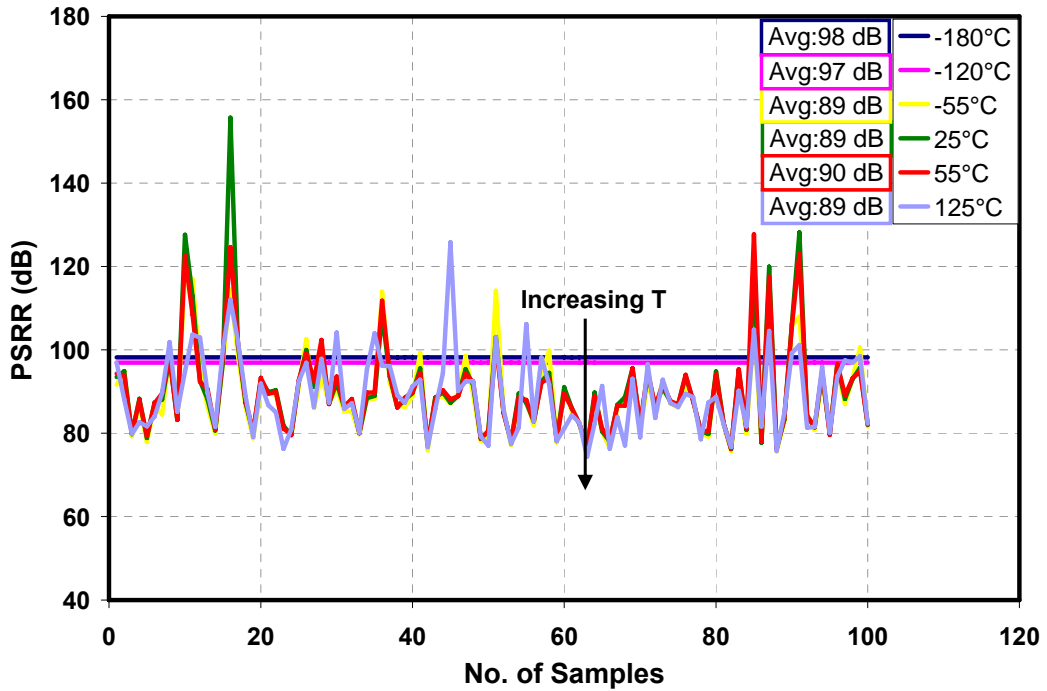


Figure 3.16 - Simulation result for PSRR across temperature

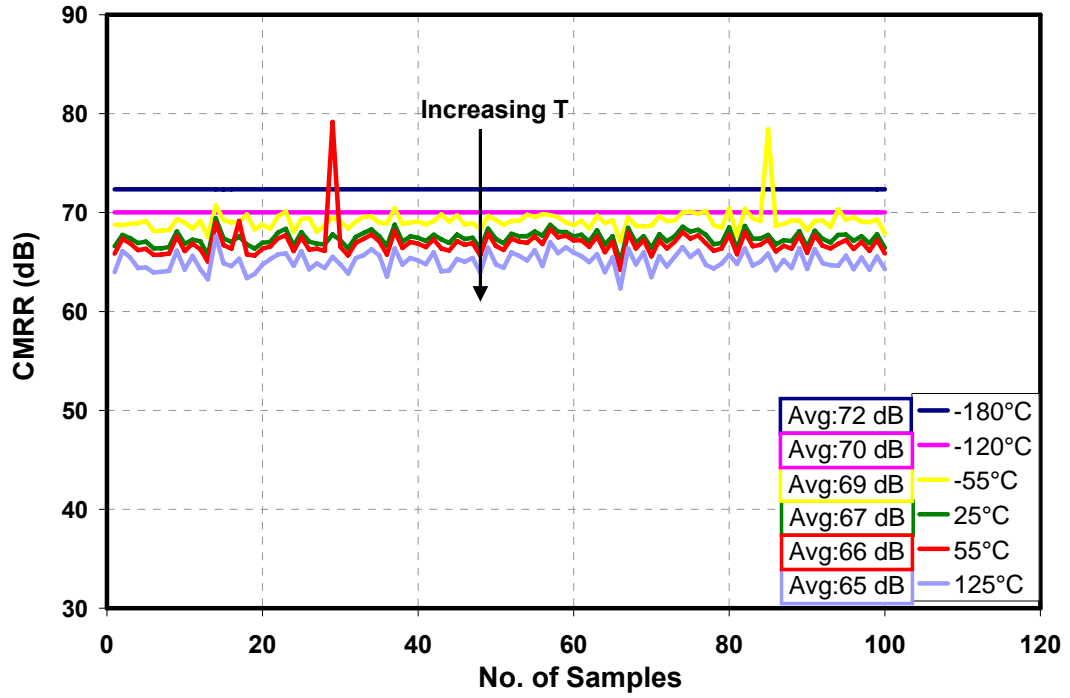


Figure 3.17 - Simulation result for CMRR across temperature

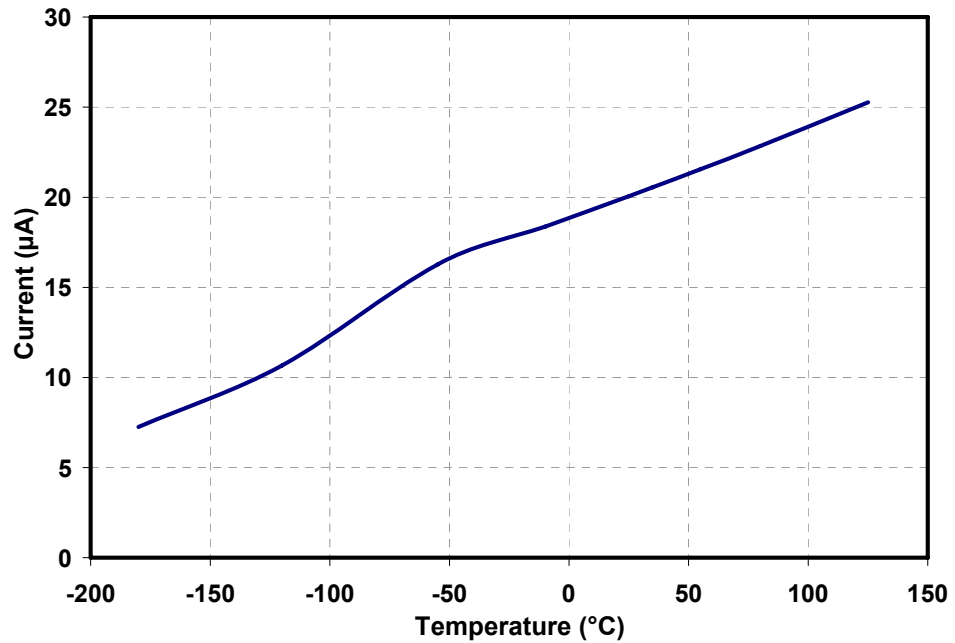


Figure 3.18 - Simulation result for constant IC current reference

3.4 Layout and Implementation

The performance of the op amp could be altered due to the presence of parasitics in the circuit layout. Therefore careful layout techniques are required in order to minimize the effect of parasitics such as capacitances, resistances, parasitic transistors, latch up etc. Guard rings with numerous substrate/well contacts around the transistors were used in order to reduce the substrate/well resistance. Doing this prevents the parasitic transistors from turning ON and thus reduces the susceptibility to latch up. Also, the generous use of substrate/well contacts minimizes the substrate noise by providing a low impedance path for the substrate noise to ground. Further, the random noise due to gate resistance is also reduced by using multi-fingered gates in the transistors.

The highly symmetrical input stage and the current mirrors require good matching between the transistors. This is achieved by the use of common centroid layout technique to match these transistors. Figure 3.19 presents the layout of the op amp. Note that the input differential pair of M_{P1} – M_{P2} is matched in common centroid. Also, the CMFB's M_{N3} along with the input current load transistors of M_{N1} and M_{N2} are matched. In the output stage, the bias transistors of M_{N4} , M_{N10} and the output drivers of M_{N5} , M_{N8} are matched together. Also, the current mirror transistors of M_{P11} , M_{P3} , M_{P6} , M_{P8} and M_{P12} are matched.

The design was implemented in a commercial, 0.35- μm 3.3-V SiGe BiCMOS process. The op amp had 6 dedicated pins for V_{IN+} , V_{IN-} , V_{OUT} , I_{BIAS} and power supply pins. The output from the current reference is connected to a pin for testing purposes and can be applied to the op amp through the I_{BIAS} pin. Figure 3.20 presents the die photograph of the fabricated chip. The op amp occupies an area of 0.075 mm².

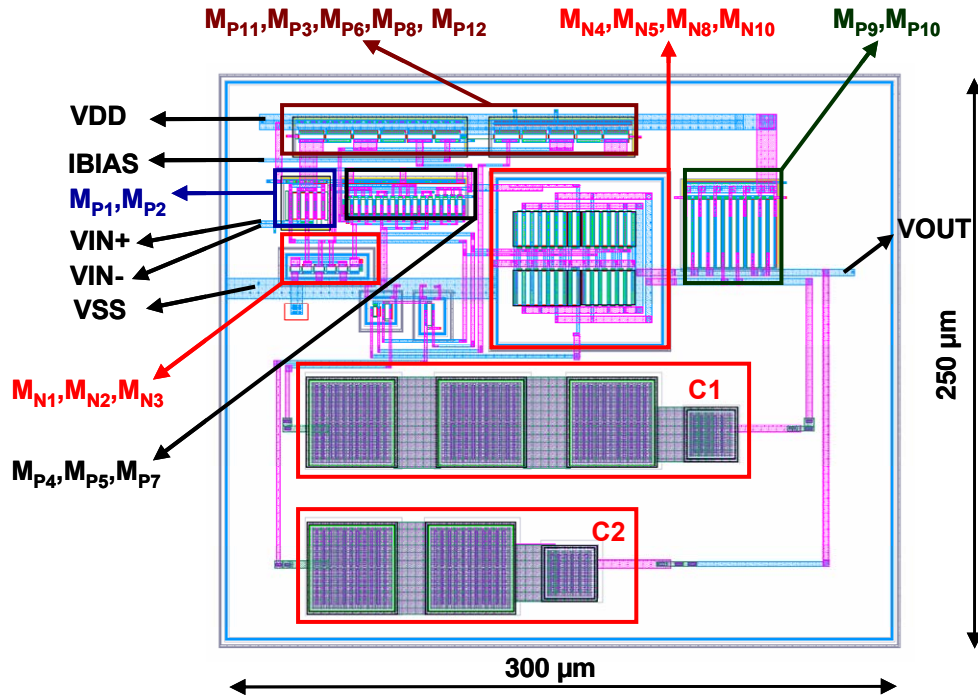


Figure 3.19 - Layout of the general-purpose op amp

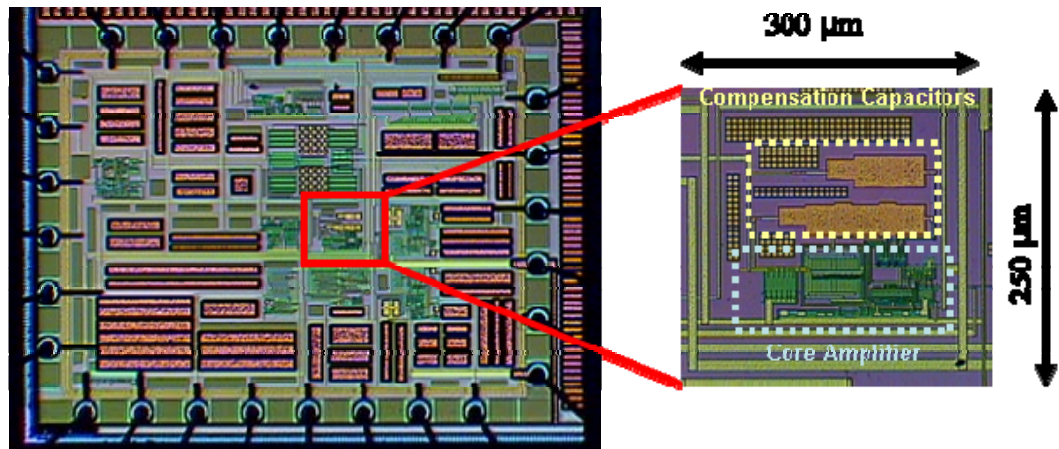


Figure 3.20 - Die photo of the general-purpose op amp

Chapter 4 Wide Temperature Range General-Purpose Op Amp – Measurement Results

This chapter presents the measurement techniques and test results obtained for the wide temperature range general-purpose operational amplifier that was tested across a temperature range of 93 K to 398 K ($-180\text{ }^{\circ}\text{C}$ to $125\text{ }^{\circ}\text{C}$). Section 4.1 discusses the setup used for characterizing the op amp across the wide temperature range. Section 4.2 illustrates the test setup and discusses the measurement results.

4.1 Temperature Testing

Figure 4.1 shows the setup used for testing across temperature. The op amp is tested by placing the chip inside a temperature chamber while the rest of the circuitry is present on a test board that is at room temperature. The temperature inside the chamber is controlled by liquid nitrogen (LN_2) coolant. With a boiling point of 77 K ($-194\text{ }^{\circ}\text{C}$), LN_2 can cool efficiently down to 93 K ($-180\text{ }^{\circ}\text{C}$) and thus sets a lower limit for testing using this setup. During its operation, the temperature chamber is not evacuated and this leads to the presence of moisture inside the chamber. In order to prevent condensation on the test chip at temperatures close to freezing point of water, the chamber is first heated to help remove moist air. At each temperature point, in order to allow thermal gradients to stabilize, an approximate wait time of 10 minutes precedes any testing. For temperatures

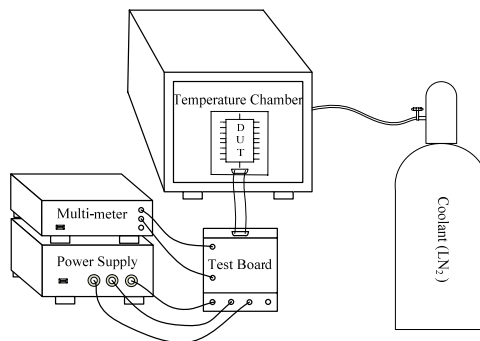


Figure 4.1- Setup for temperature testing

below 93 K, tests were performed in the cryogenic test system at the Georgia Institute of Technology in Atlanta. Their system operates in vacuum and uses liquid Helium coolant to achieve 4 K ($-269\text{ }^{\circ}\text{C}$).

4.2 Test Setup

The test circuits necessary for characterizing the op amp were built on a printed circuit board, shown in Appendix, Figure A.3, and used to test the op amp at room temperature. Complementary supply voltages of $\pm 1.65\text{ V}$, from an Agilent E3631A, were used to simplify testing by referencing the signals to a mid-supply voltage of ground. Power supply bypassing capacitors were placed close to the supply pins of the op amp to dampen any ac ripple and power supply noise. To filter out the power supply noise over a wide bandwidth, an array of capacitors comprising of an electrolytic $100\text{ }\mu\text{F}$, tantalum $1\text{ }\mu\text{F}$ and ceramic $0.1\text{ }\mu\text{F}$ were used. The op amp was biased by a $10\text{ }\mu\text{A}$ current sink which was provided by the constant-IC current reference circuit, also fabricated in the same chip. The output from the current reference of $20\text{ }\mu\text{A}$ is available at an output pin and this current was fed to the op amp through another dedicated pin which supplies the required bias current to the op amp by internally mirroring the $20\text{ }\mu\text{A}$ to $10\text{ }\mu\text{A}$. If required, an external source of current biasing can also be supplied through this pin. An effective load capacitance of about 50 pF was connected to the op amp's output for all test configurations. An oscilloscope probe with a load of 15 pF , $10\times$ attenuation, and $1\text{ M}\Omega$ impedance was used for all measurements (included in the 50 pF load estimate). A sample of 5 chips was used for testing and the measurements results obtained show consistent trend in the changes across the temperature range.

The setup to measure the systematic offset voltage has the op amp configured with a non-inverting gain of 1,000 and a grounded positive input terminal as shown in Figure 4.2. Using the Agilent 34401A multimeter, the offset V_{OUT} was measured for different chips. The average measured offset voltage for 5 chips at $25\text{ }^{\circ}\text{C}$ is 1.62 mV and this matches well with the Monte Carlo simulated value of 1.3 mV . The change in the magnitude of V_{OS} across temperature is plotted in Figure 4.3. The low offset can be

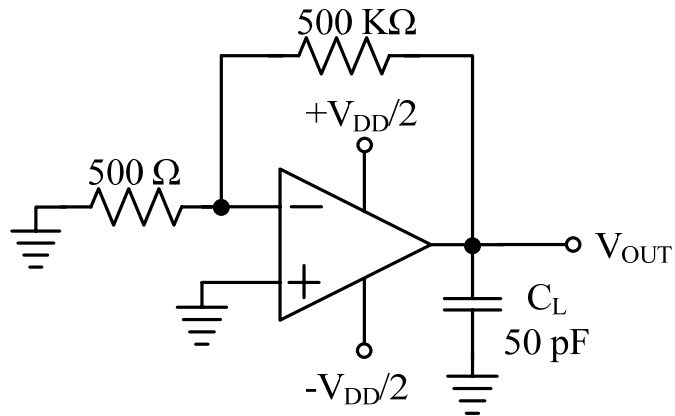


Figure 4.2 - Measurement setup for offset voltage

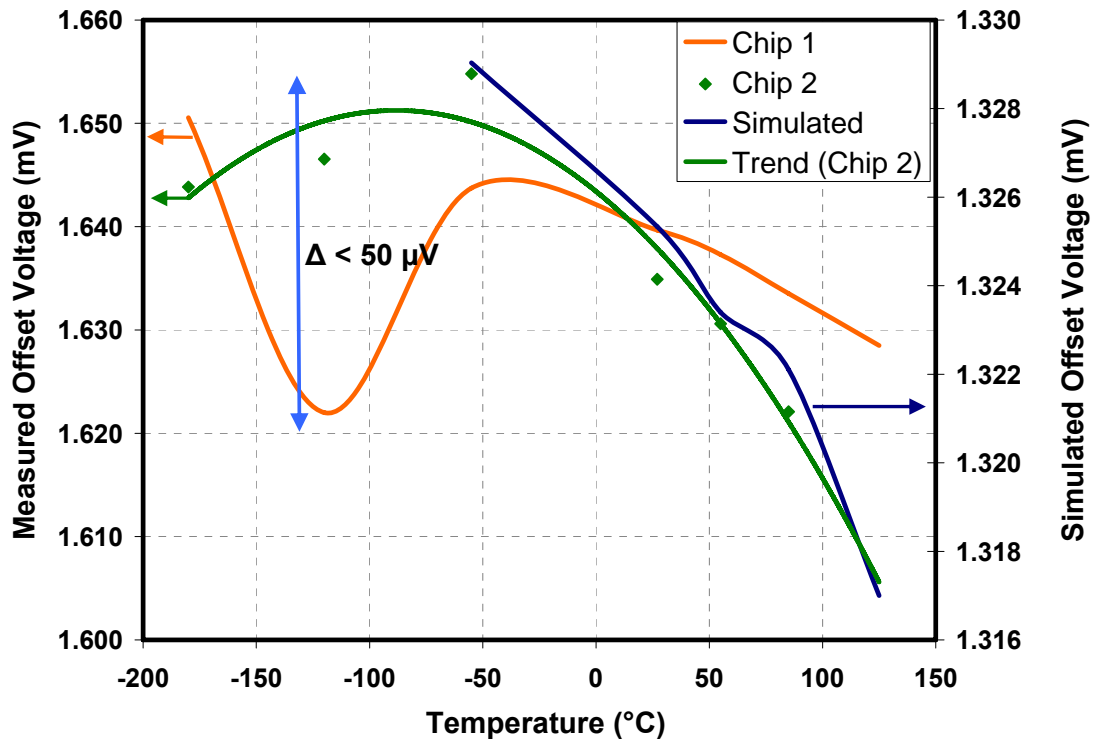


Figure 4.3 - Measured V_{OS} across temperature

attributed to the highly symmetrical input stage design, CMFB action, and good matching provided by the common centroid layout technique. Thanks to the CMFB circuit, the variation of the offset voltage across temperature is minimal and is measured to be less than 50 μV and the drift is computed to be 85 $\text{nV}/^\circ\text{C}$.

The ICMR is measured by configuring the op amp as a non-inverting unity gain buffer as shown in Figure 4.4. A linear input ranging from V_{SS} to V_{DD} is applied to the op amp and the output voltage is monitored. The range of input voltages for which the slope of the output voltage is unity represents an estimate of the ICMR. At 25 $^\circ\text{C}$, the measured ICMR extends from 0 to 2.9 V which matches well with the simulated result of 0 to 3 V. The lower range of ICMR extends to ground for the complete temperature range. Figure 4.5 shows the measured ICMR maximum voltage with variation in temperature. The maximum range of ICMR decreases at LT due to the increase in V_{TH} .

The open-loop gain of an op amp can be defined as

$$A_{OL} = \frac{V_{OUT}}{V_\epsilon} \quad (4.1)$$

where V_{OUT} is the op amp's output voltage, which is assumed to be zero when no input is applied and V_ϵ is the feedback error voltage, which is the input differential voltage applied to the amplifier [36]. Due to the very high differential gain of the op amp, measuring the gain using an open-loop configuration is very difficult, so the op amp is kept in a closed-loop configuration.

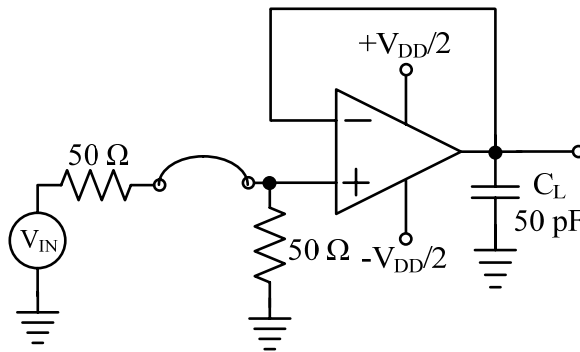


Figure 4.4 - Measurement setup for ICMR

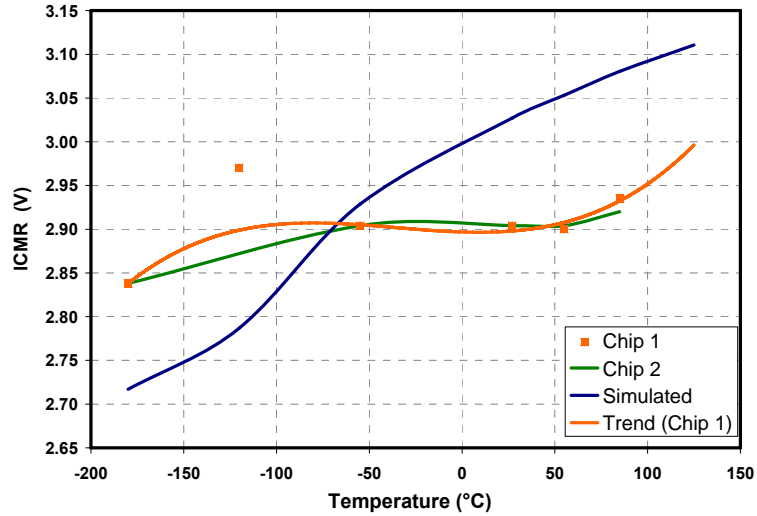


Figure 4.5 - Measured ICMR max across temperature

Figure 4.6 presents the setup used for the open-loop gain measurement where the op amp is configured as a unity-gain amplifier. The signal is applied to the negative input terminal while the positive input is grounded, thereby maintaining a fixed common-mode voltage of ground, and therefore the finite open-loop gain can be differentiated from the finite CMRR [36]. A large feedback resistor is chosen to prevent dc loading of the op amp's output. The probing of the error voltage V_e at the negative input terminal of the op amp introduces capacitance at the node which, along with the large input resistance, would form a low-frequency pole and thereby cause instability. Capacitor C_1 fixes the location of the input pole and capacitor C_F adds a zero to improve the stability of the system.

An SR770 network analyzer, which provides high resolution voltage measurements, was used for the voltage measurements. The network analyzer has an internal sine-wave synthesizer which is perfectly synchronized with the timing window of the FFT analyzer. Using this sine wave as the op amp's input prevents any spectral leakage during the FFT analysis of the op amp's output and thereby gives an accurate measurement. A nominal input of 200 mV was applied for the measurements. The SR770 has a frequency limit of 100 kHz, so the op amp's open-loop gain was characterized for this range and unity gain bandwidth was derived by extrapolating the plot with a 20 dB/decade slope to cross the 0 dB line. Figure 4.7 shows the measured open-loop gain

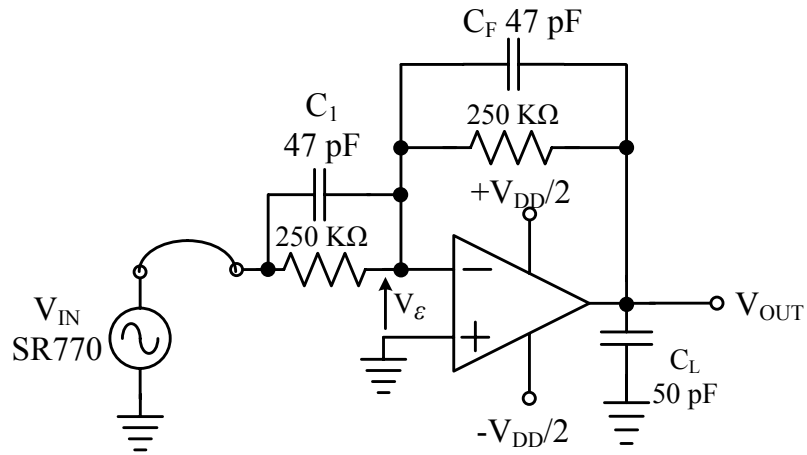


Figure 4.6 - Open-loop gain measurement circuit

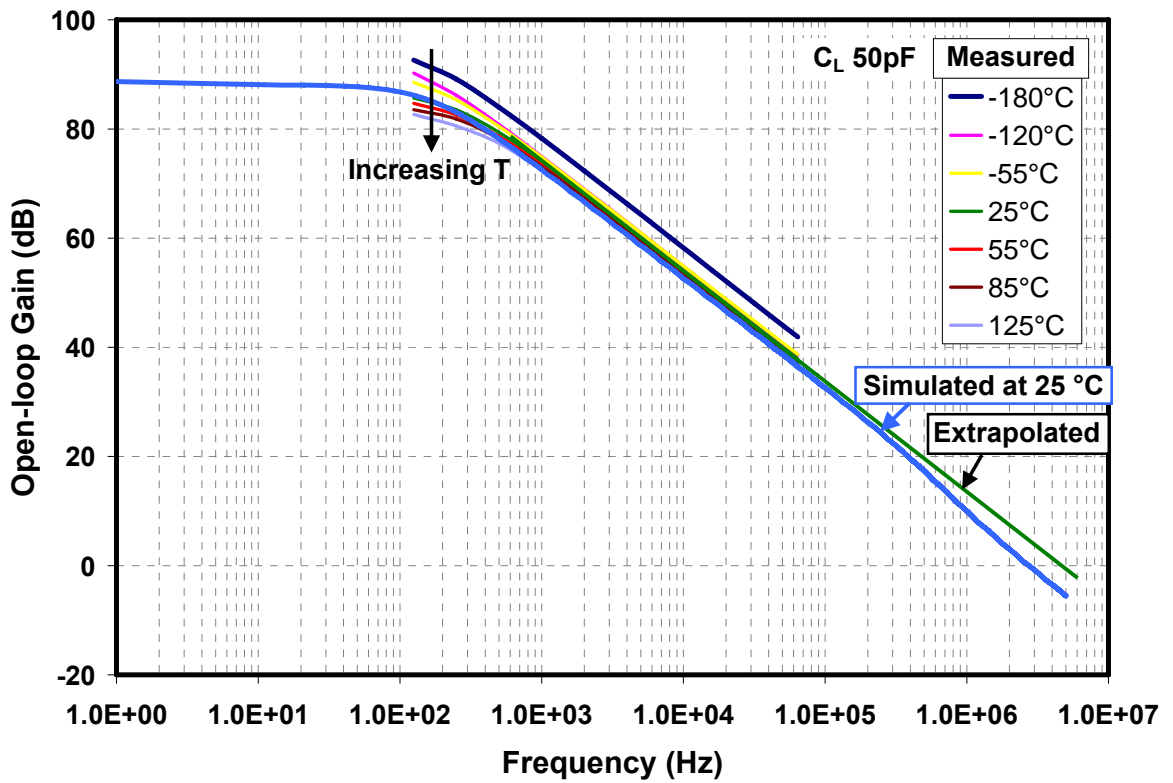


Figure 4.7 - Measured results for open-loop gain across temperature

across temperature along with the simulated data across the temperature range. Note that the improvement in g_m at LT increases the A_{OL} . The measured open-loop gain reaches 85 dB which matches very closely with the simulated result of 89 dB. The extrapolated UGBW is 4.5 MHz which is more than the simulated value of 2.75 MHz. This discrepancy is due to mismatch in the relative positions of the non-dominant poles and zeros. Any mismatch in the current mirror of the output drivers (M_{P9} , M_{P10} , M_{N4} , M_{N5} , M_{N8} of Figure 3.3) could cause a change in g_m and thus affect the location of the poles and zeros.

The op amp's response to small-signal and large-signal transient inputs is essential in determining the rise time, fall time and the slew rate of the op amp. The small-signal analysis also provides information about the small-signal -3dB BW and the phase margin of the amplifier. To perform transient analysis, the op amp is configured as a unity-gain non-inverting buffer as shown in Figure 4.4.

For small-signal analysis, a square wave of 100 mV_{pp} is input to the op amp and the rise, fall times along with the respective overshoots are measured. The small-signal BW, which is the UGBW, is derived from the rise time using the first-order system approximation of [37],

$$UGBW = \frac{0.35}{t_{rise(10\%-90\%)}} \quad (4.2)$$

Figure 4.8 shows the change in UGBW across temperature. With reduction in temperature, the increase in g_m is expected to increase the UGBW. But, the measured UGBW at -180 °C is less than that at -120 °C and the UGBW seems to start falling beyond this temperature. This is due to the approximation involved in deriving the UGBW values. The measured BW varies less than 20% from the simulated result.

In order to improve the results, an alternate setup was used to directly measure the small-signal bandwidth using the op amp in non-inverting unity gain configuration as in Figure 4.4. A sinusoidal input waveform of 100 mV was input to the op amp. The frequency of the input sinusoidal signal was increased to determine the 3 dB bandwidth of the op amp. Figure 4.9 shows the measured results across temperature. As expected, the measured UGBW increases with reduction in temperature in both the samples.

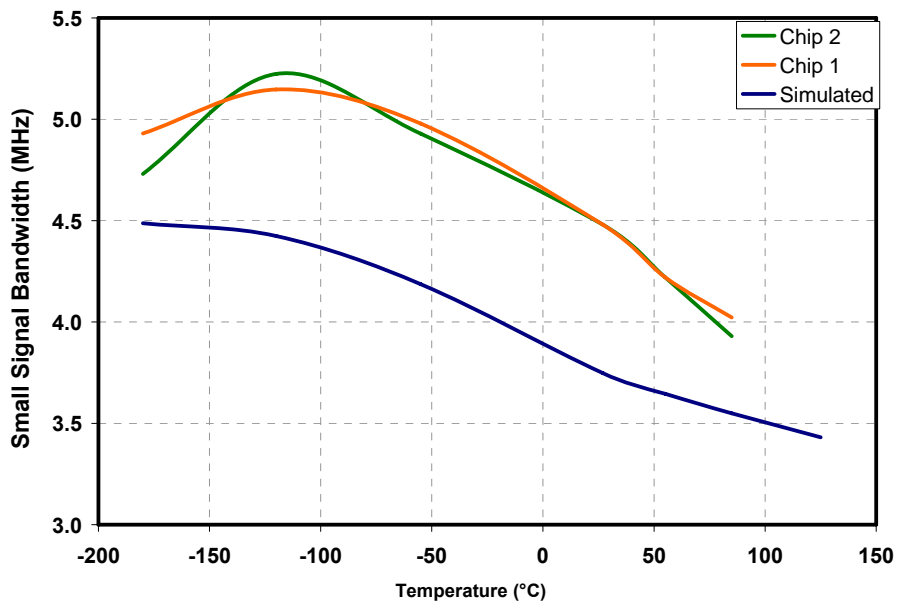


Figure 4.8 - Measured UGBW across temperature

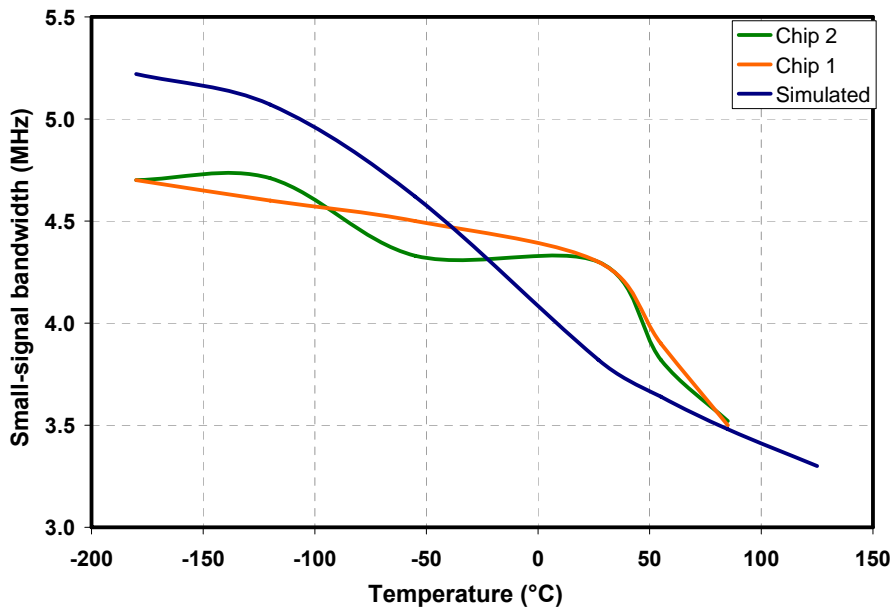


Figure 4.9 - Measured UGBW across temperature using sinusoidal input signal

Also, the measured results vary less than 10 % from the simulated results.

The phase margin (PM) of the system is determined using the measured percentage overshoot value [37]. For the five chip sample, at 25 °C, the PM is about 62° for a 50 pF load. For a PM of 45°, the op amp is capable of driving a capacitive load of about 110 pF across the temperature range. Figure 4.10 shows a comparison between the simulated and measured PM across temperature and the maximum change is less than 30%.

Slew Rate (SR) is measured using large-signal analysis by applying a 1 V_{pp} input at 1 kHz to the op amp, which is configured as a unity-gain non-inverting buffer. Figure 4.11 and Figure 4.12 present the positive and negative slewing signals of the large-signal analysis. Figure 4.13 shows the slew rate vs. temperature characteristics of the amplifier. The measured values show higher SR from -55 °C to 125 °C when compared to simulation. This is due to the increase in the current generated by the current reference from a simulated value of 20 μA to the measured value of 25 μA at 25 °C, as shown later in the results for constant-IC current reference. The ratio of SR increase matches well with that of the current.

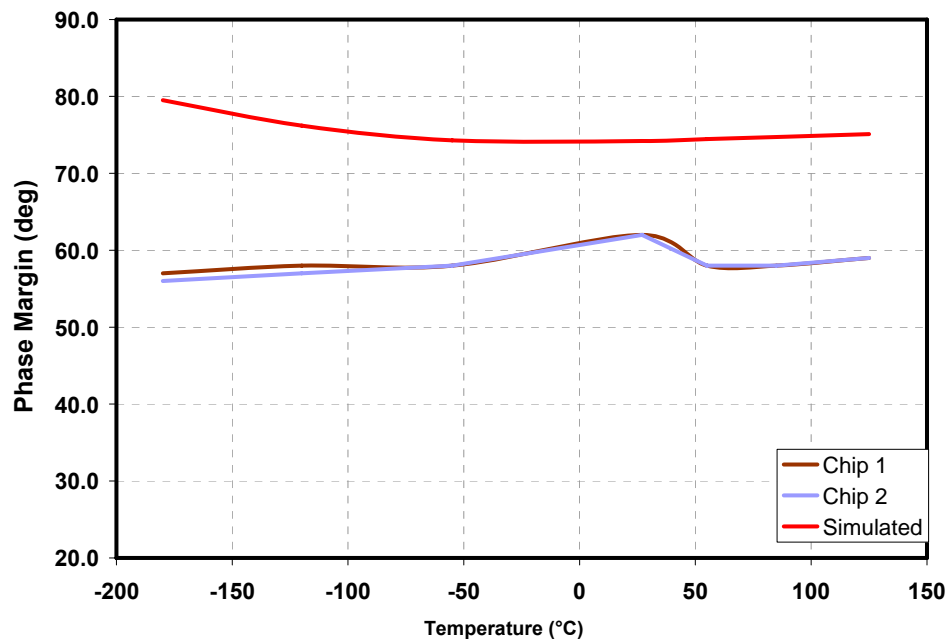


Figure 4.10 - Measured phase margin across temperature

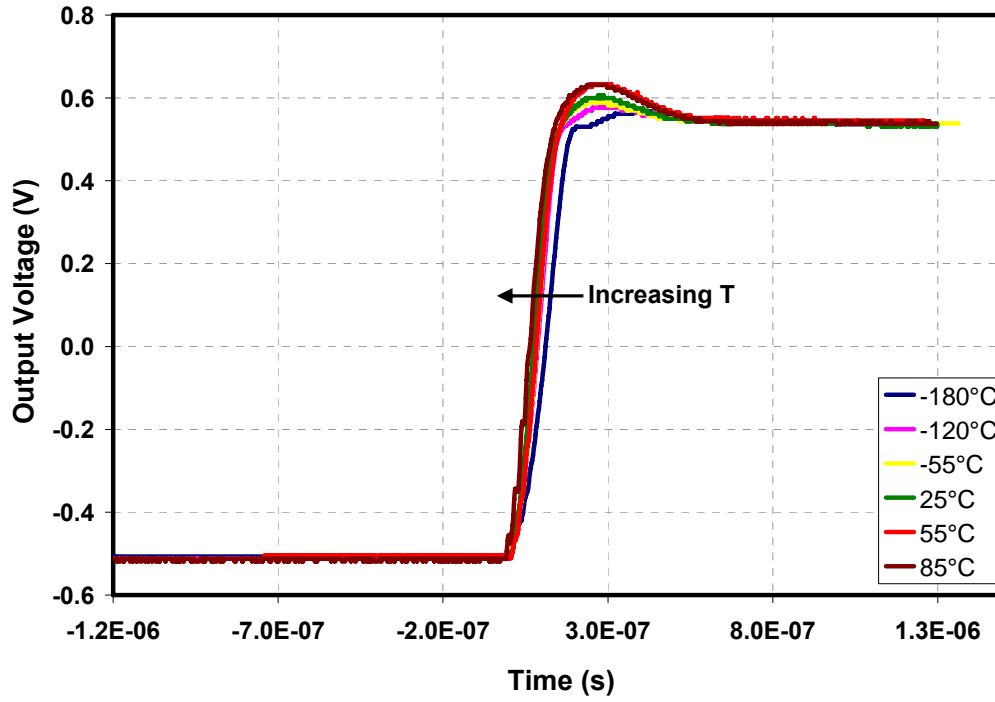


Figure 4.11 - Measured positive slewing edge across temperature

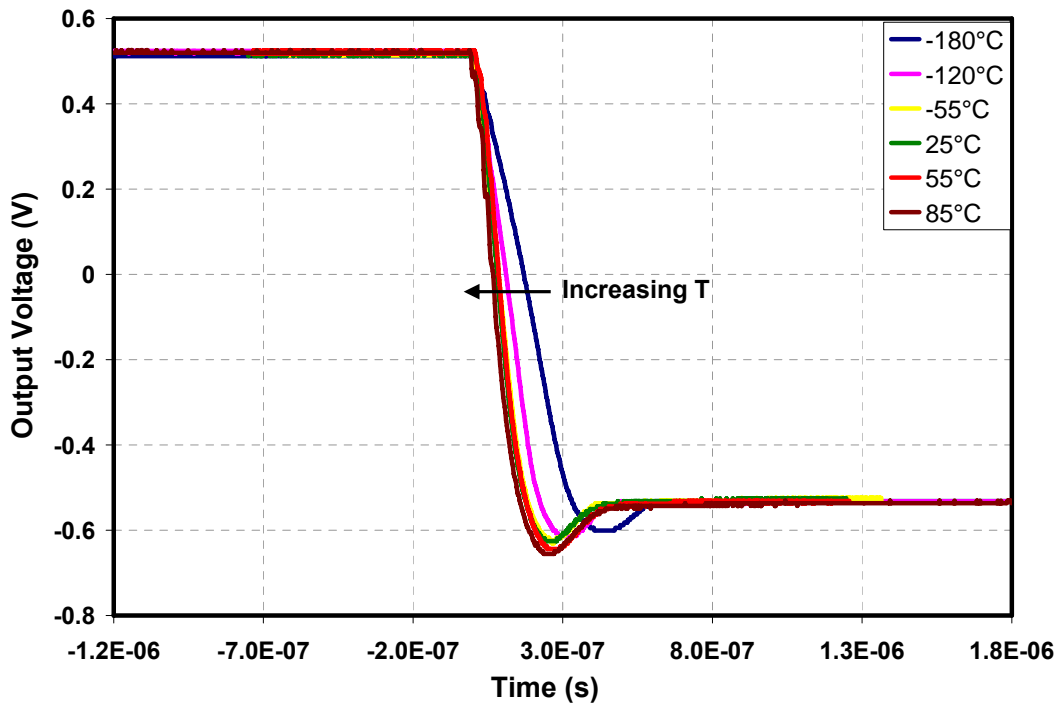


Figure 4.12 - Measured negative slewing edge across temperature

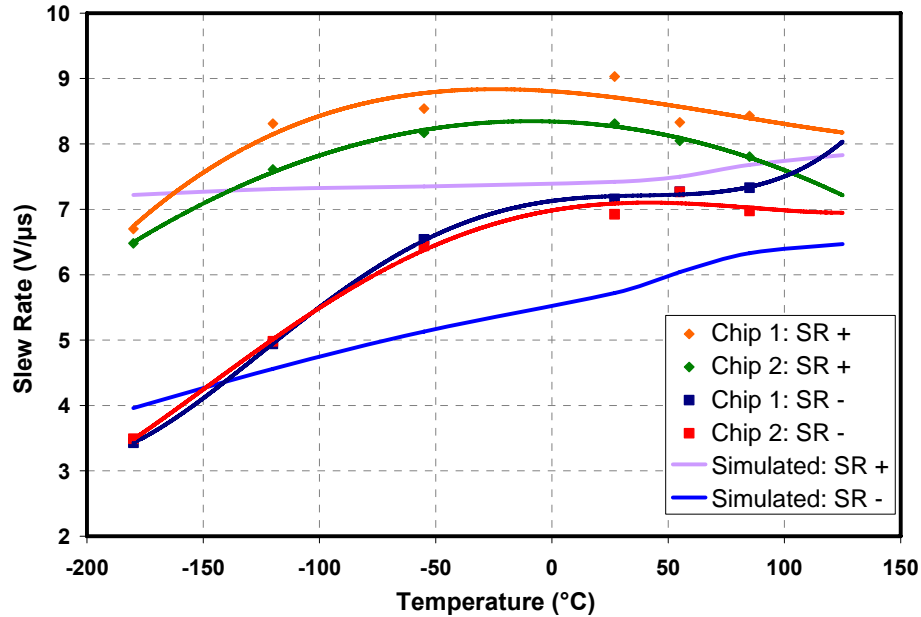


Figure 4.13 - Measured slew rate across temperature

The input referred noise of an op amp can be measured using the schematic as in Figure 4.14. The output noise of the op amp is amplified by a low-noise preamplifier (Perkin Elmer 5183) and the output noise spectral density is measured using the HP3985A network analyzer. The preamplifier provides a gain of 60 dB, a usable bandwidth limit of 1 MHz, and a typical input referred noise of $2 \text{ nV}/\sqrt{\text{Hz}}$ at 1 KHz. Hence the op amp is the dominant noise source in this setup. Noise measurements were performed for a frequency range of 10 Hz to 1 MHz, with an average of 50 data points per decade for frequencies above 10 KHz. The n/w analyzer was configured and the data was processed using software based on Lab View [39]. In order to verify the accuracy of the measurement setup, the noise voltage for 1 K Ω resistor was measured. The measured noise floor was $4 \text{ nV}/\sqrt{\text{Hz}}$ which is the expected thermal noise voltage for the resistor.

The measured input referred noise of the op amp is shown in Figure 4.15. The noise characteristic is consistent across the 5 chips. At 25 °C, the input referred noise at 100 KHz is about $36 \text{ nV}/\sqrt{\text{Hz}}$ which is much less than the simulated value of $67 \text{ nV}/\sqrt{\text{Hz}}$. This difference is due to the pessimistic noise model used in the simulations. Note that, as in the simulation results of Figure 3.15, the flicker noise corner frequency is more than 1 MHz. Also, the noise increases at high temperatures due to an increase in thermal noise.

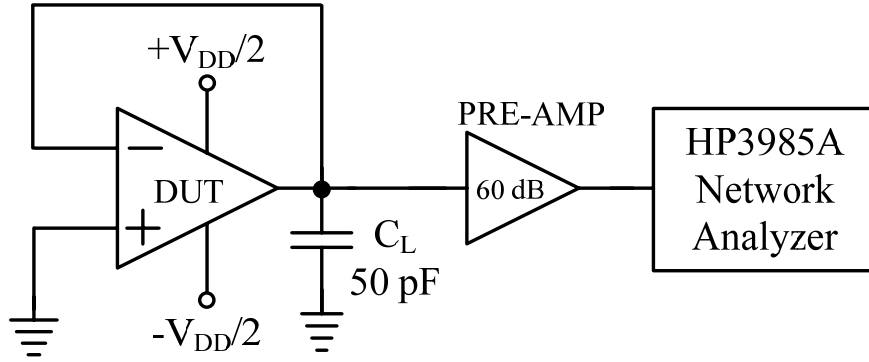


Figure 4.14 - Setup for noise measurement

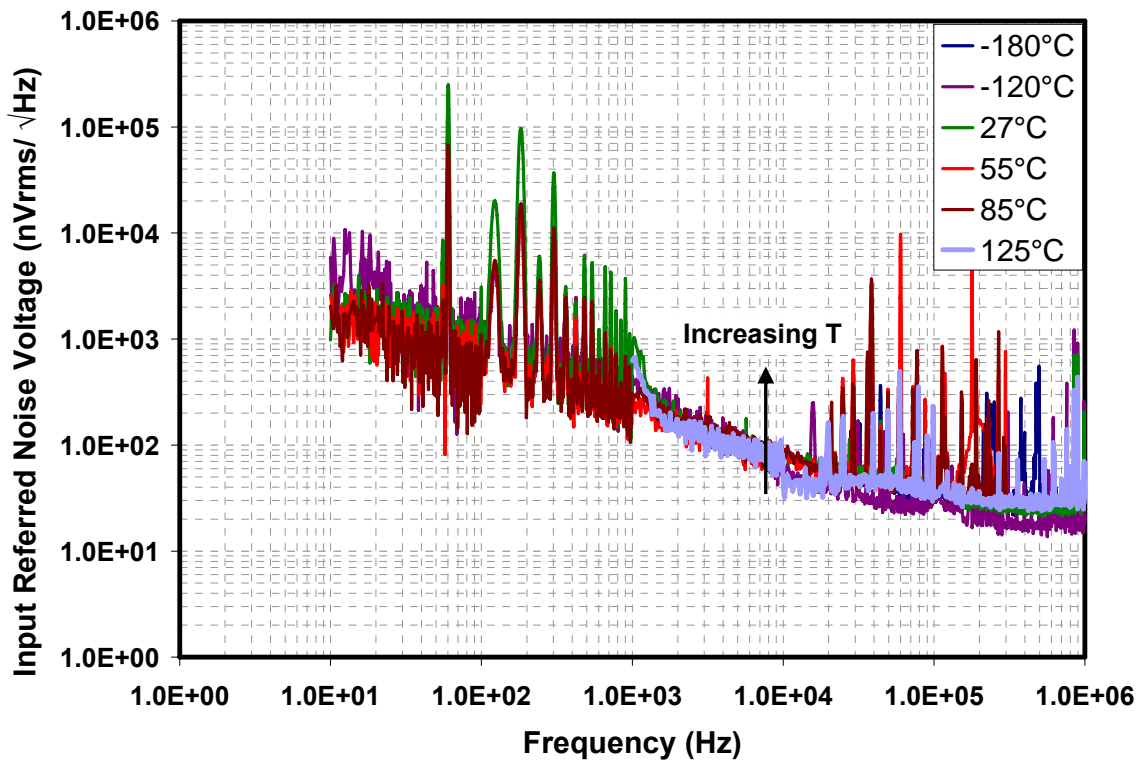


Figure 4.15 - Measured input referred noise voltage across temperature

PSRR is represented as the ratio of change in power supply voltage to the change in the op amp's output, caused by the power supply change. This change in the output can be attributed to the bias point variation with the power supply changes, causing a change in the offset voltage. Thus PSRR can be measured as,

$$PSRR = \frac{\Delta V_{PS}}{\Delta V_{OUT}} = \frac{\Delta V_{PS}}{\Delta V_{OS}} \quad (4.3)$$

The schematic in Figure 4.16 presents the measurement method to characterize the DC PSRR. The op amp is powered with complementary power supplies and is configured in unity-gain mode with the common-mode voltage set at mid-supply voltage of ground. To determine the PSRR, the supply voltages are varied and the V_{OS} which is the output of op amp is measured at each point and PSRR is computed using equation (4.3).

Figure 4.17 presents the measured DC PSRR across the temperature range. The DC PSRR was characterized for a $\pm 10\%$ variation of the supply voltages using Lab View [40]. The measured PSRR at 25 °C is 65 dB which is less than the expected value of 89 dB. This discrepancy could be due to limitations involved in measuring the minute variations of the offset voltage and also due to inaccurate simulation results caused by inadequate MOSFET mismatch modeling.

CMRR is defined as the ratio of the voltage gain for a differential-mode input

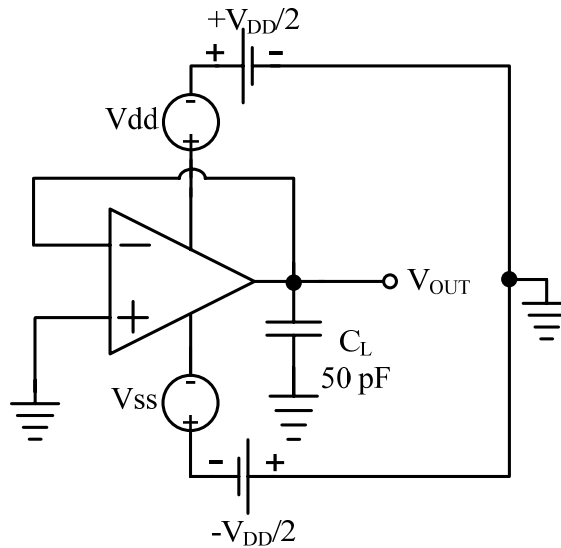


Figure 4.16 - PSRR measurement circuit

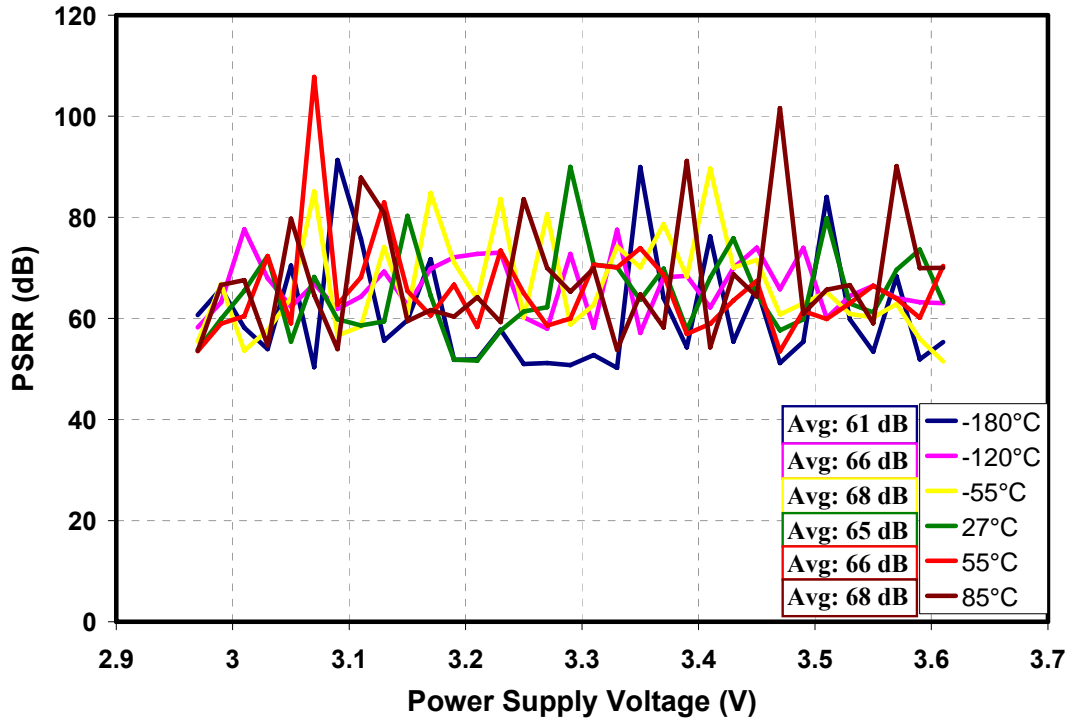


Figure 4.17 - Measured PSRR across temperature

signal to the voltage gain for a common-mode input signal, and can be stated as

$$CMRR = \frac{A_{DM}}{A_{CM}} = \frac{\left[\frac{\Delta V_{OUT}}{\Delta V_{IND}} \right]}{\left[\frac{\Delta V_{OUT}}{\Delta V_{INCM}} \right]} = \frac{\Delta V_{INCM}}{\Delta V_{IND}} \quad (4.4)$$

Therefore, measuring the dc CMRR involves in determining the change in the offset voltage due to any change in the applied common-mode voltage. But, power supply voltage variation would affect the output as well as the offset voltage. In order to ensure that the measured change in the offset voltage is only due to a change in common-mode input voltage, the output voltage of the op amp is maintained at a fixed voltage for the complete test sequence. Figure 4.18 illustrates the test circuit used in the measurement [36]. By using a driver, the op amp's output voltage is maintained at ground, irrespective of the value of the power supply or the common-mode input voltage. The common-mode voltage, V_{CM} is varied across the op amp's ICMR range and the change in offset voltage is captured. Figure 4.19 presents the CMRR across the common-mode voltage variations

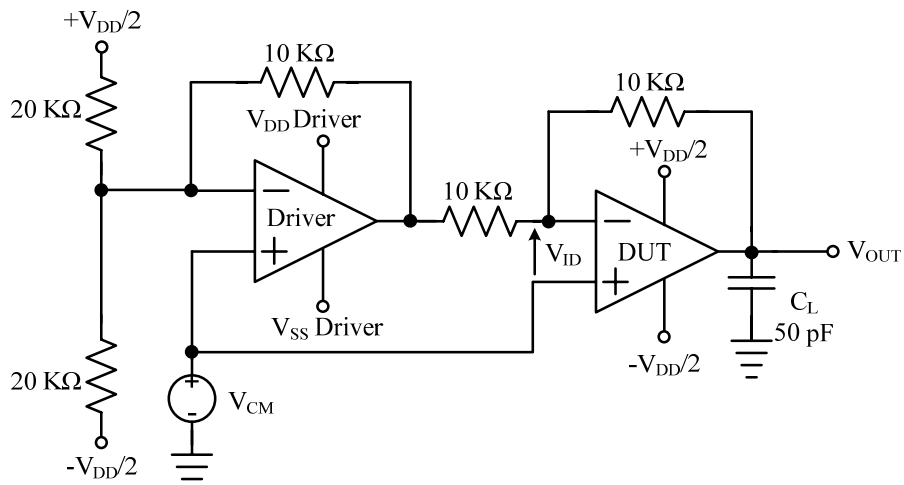


Figure 4.18 - CMRR measurement circuit

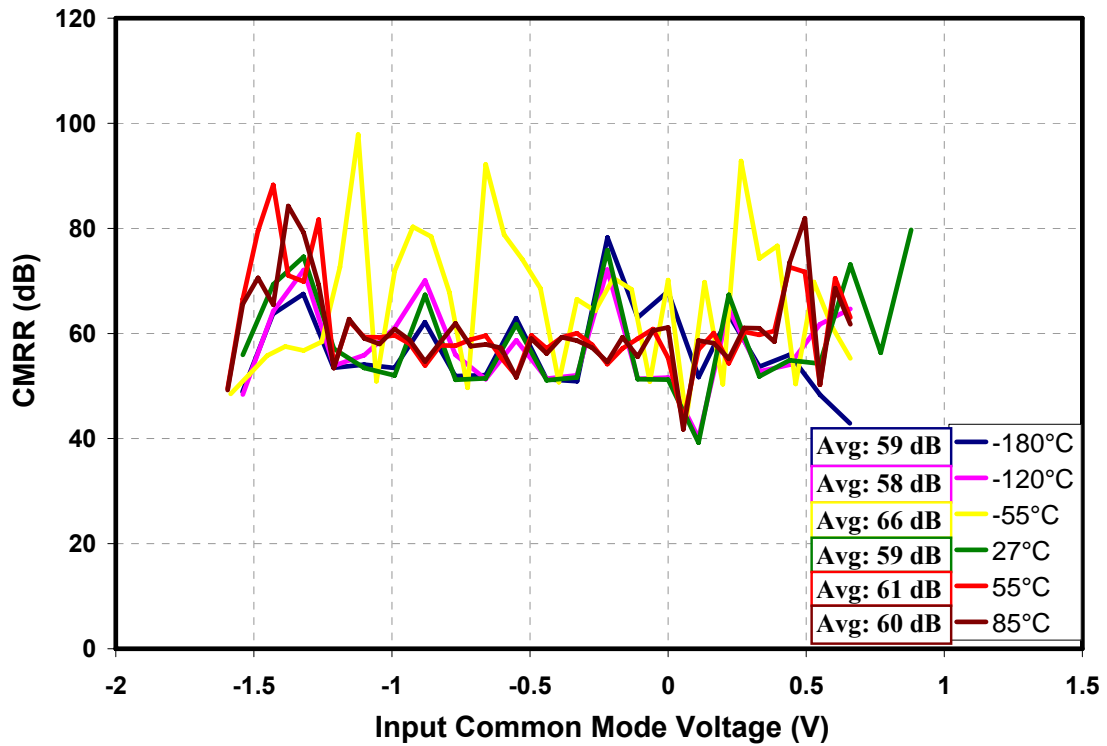


Figure 4.19 - Measured CMRR across temperature

across temperature. The measured CMRR values match well with those from Monte Carlo simulations.

Figure 4.20 shows the measured bias current from the constant IC current reference circuit vs. Temperature.

4.3 Summary

From the measured results, it is shown the op amp provides a high gain of 85 dB and is capable of driving large capacitive loads of up to 110 pF with a phase margin of 45° across temperature. The op amp also offers good dynamic range with its input ground sensing capability, rail-to-rail output swing and low offset voltage. The use of CMFB has reduced the offset and provided very low offset drift of about 85 nV/°C. Further, the measured input referred noise voltage is better than expected. The op amp has a low power consumption of about 1.3 mW at 25 °C.

On the whole, the general purpose op amp works as designed, across the temperature range of -180 °C to 125 °C, and the measurement results match well with the simulation.

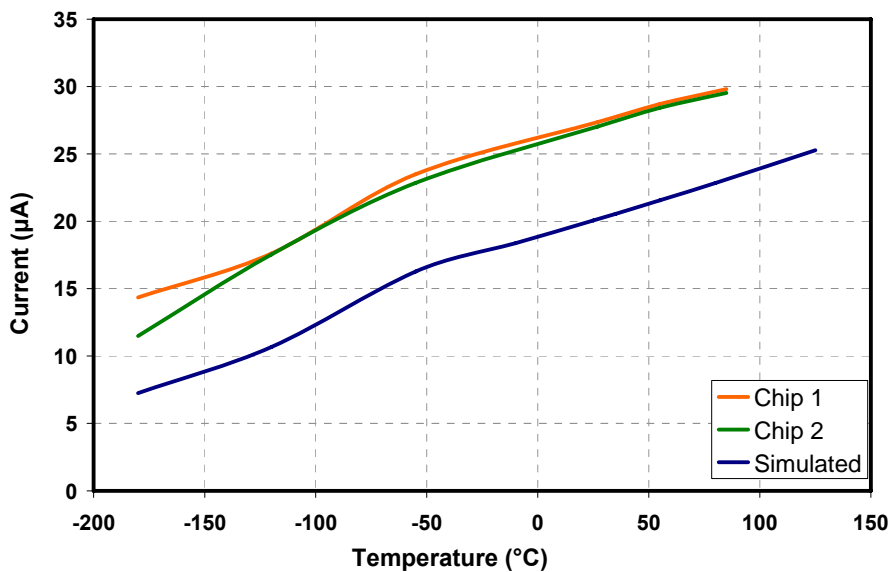


Figure 4.20 - Measured bias current vs. temperature

Chapter 5 Conclusions

5.1 Conclusions

This thesis presents the design and analysis of a general purpose op amp suitable for operation in extreme temperature environments. This work also investigates the effect of temperature variation on the performance of MOS devices and circuits. The measurement results confirm that the op amp performs as expected across the temperature range of $-180\text{ }^{\circ}\text{C}$ to $125\text{ }^{\circ}\text{C}$.

From the measured results, it is illustrated that the op amp provides high gain, has ground sensing ICMR, rail-to-rail output swing, low offset and low power consumption. It has good current driving capability and can drive up to 110 pF load with a phase margin of 45° across temperature. Further, the measured input referred noise voltage is better than expected. The use of CMFB has reduced the offset voltage and rendered a minimal offset drift with temperature of about $85\text{ nV}/^{\circ}\text{C}$. Thus the op amp is suitable for use in a wide range of analog signal processing applications across extreme temperatures.

This work also demonstrates that minimum variation in the op amp's performance can be achieved, across a large variation in temperature, by biasing the CMOS devices in a constant inversion-coefficient current for the desirable temperature range.

5.2 Future Work

The future work on this thesis can be aimed at understanding certain aspects of the circuit and enhancing the characterization of the op amp at cryo temperatures. The following discussion presents an outlook to the possible enhancements to this work.

5.2.1 Circuit-level

Certain aspects of the circuit such as the PSRR, the CMFB action on the CMRR could be further investigated to better understand the circuit. The discrepancy between the measured and simulated values of phase margin and PSRR could be examined in more detail. Simulating the op amp's PSRR by utilizing the EKV model, which

incorporates an accurate MOSFET mismatch model, might help in improving the accuracy of PSRR simulations. A study of EKV and the BSIM models could also give more insight into the circuit operation. A revised test setup could be used to characterize the PSRR and CMRR as a function of frequency.

5.2.2 System-level

This work is intended for use in space applications, specifically in lunar missions where the temperature inside lunar craters can go down to $-230\text{ }^{\circ}\text{C}$. Therefore it is essential to investigate the op amp's operation across wide temperature swings ranging from $-230\text{ }^{\circ}\text{C}$ to $120\text{ }^{\circ}\text{C}$ and as well as in radiation intense environments. With this focus, the op amp was tested at $-230\text{ }^{\circ}\text{C}$ in the cryogenic test system at the Georgia Institute of Technology in Atlanta. The test results proved that the circuit is fully functional at $-230\text{ }^{\circ}\text{C}$. Although the op amp operates satisfactorily in the desirable temperature range and the degradation effects due to the extreme temperature operation were not noticeable, further verification is needed before assuring the long-term operability of the circuit. The accumulative effects of temperature variation on the lifetime of the devices due to degradation mechanisms such as hot carrier effects, oxide breakdown and carrier freeze out have to be evaluated especially for operations below $-180\text{ }^{\circ}\text{C}$.

Additionally, to study the impact of radiation exposure on the performance of the op amp, the circuit was irradiated with 63 MeV protons at $25\text{ }^{\circ}\text{C}$ at the Crocker Nuclear Laboratory at UC Davis. The samples were subjected to 3 different dosage levels of 30, 100 and 300 Krads. Preliminary measurement results at $25\text{ }^{\circ}\text{C}$ show minimal variations in the op amp performance when compared to the pre-radiation results. Device level characterization could be done to study the degradation in mobility, g_m , and reduction in threshold voltage due to radiation. Temperature testing is yet to be performed on these irradiated samples and a thorough analysis of the results is necessary to determine the radiation tolerance of the circuit.

Also, in order to suit the application, modifications could be made to the op amp circuit to improve its performance. For instance, a buffer stage could be added at the output to improve the drive capability of the op amp.

REFERENCES

- [1] Bruce Carter and Thomas R. Brown, "Handbook of Operational Amplifier Applications", Application Report, Texas Instruments, Oct. 2001.
- [2] John D. Cressler, "On the Potentials of SiGe HBTs for Extreme Environment Electronics" Proceedings of the IEEE, Vol. 93, No. 9, pp. 1559-1582, Sep. 2005.
- [3] The NASA, Mars Exploration Rover Mission, <http://marsrovers.nasa.gov/mission/>
- [4] John D. Cressler and SiGe Code TTeam, "SiGe Code T Project: Month 4 Review" Oct. 2005.
- [5] Gray, Hurst, Lewis, Meyer, "Analysis and Design of Analog Integrated Circuits", Wiley, New York, 2001.
- [6] Jim Karki, "Understanding Operational Amplifier Specifications", Digital Signal Processing Solutions, Apr. 1998.
- [7] E. J. Kennedy, "Operational Amplifier Circuits, Theory and Applications", Holt, Rinehart and Winston, Inc, New York, 1988.
- [8] F. H. Gaensslen, D. D. Meyer, "Liquid Nitrogen CMOS for Computer Applications", IEEE International conference on Computer Design, pp. 4-8, Oct. 1991.
- [9] G. Ghibaudo, F. Balestra, "Low Temperature Characterization of Silicon CMOS Devices", IEEE International Conference on Microelectronics, Vol. 2, pp. 613-622, Sep. 1995.
- [10] William F. Clark et al, "Low Temperature CMOS – A Brief Review", IEEE Transactions on Components, Hybrids, and Manufacturing Technology, Vol. 15, No. 3, pp. 397- 404, Jun. 1992.
- [11] F. H. Gaensslen et al, "Very small MOSFETs for Low Temperature Operation", IEEE Transaction on Electron Devices, Vol. ED-24, No. 3, pp. 218- 229, Mar. 1997.
- [12] Raymond Wang et al, "Threshold Voltage Variations with Temperature in MOS Transistors", IEEE Transactions on Electron Devices, Vol. 18, Issue 6, pp. 386-388, Jun. 1971.
- [13] Stephen C. Terry et al, "Development of Robust Analog Electronics at the University of Tennessee for NASA/JPL Extreme Environment Applications", Proceedings of the 15th Biennial University/Government/Industry Microelectronics Symposium, pp. 124-127, Jun. 2003.

- [14] Robert M. Fox, Richard C. Jaeger, "MOSFET Behavior and Circuit Considerations for Analog Applications at 77K", IEEE Transactions on Electron Devices, Vol. ED-34, No. 1, pp. 114-123, Jan. 1997.
- [15] S. T. Gunaseelan et al, "Low Temperature Performance of Operational Amplifiers for Space Applications", IEEE CCECE, Vol. 1, pp. 231-234, May 2003.
- [16] Neil H. E. Weste, David Harris, "CMOS VLSI Design, A Circuits and Systems Perspective", Pearson Education, 2005.
- [17] C. R. Viswanathan, "Low Temperature Characterization of CMOS Devices", International Symposium on VLSI Technology, Systems and Applications, pp. 207-212, May 1989.
- [18] F. S. Shoucair, "Potential and problems of high-temperature electronics and CMOS integrated circuits (25-250 °C) – an overview", Microelectronics Journal, Vol. 22, No.2, pp.39-54, 1991.
- [19] F. S. Shoucair, "Design considerations in High Temperature Analog CMOS Integrated Circuits", IEEE Transactions on Components, Hybrids, and Manufacturing Technology, Vol. CHMT-9, No.3, pp.242-251, Sep. 1986.
- [20] J.Bergmann and A.ten Have, "High Temperature Operational Amplifier with low offset voltage", IEEE Proceedings of URSI International Symposium on Signals, Systems and Electronics, pp.451-454, Oct. 1995.
- [21] Ashraf A.Osman et al, "Investigation of High Temperature Effects on MOSFET Transconductance (gm)", Fourth Intl. High Temperature Electronics Conference, pp.301-304, Jun. 1998.
- [22] Philip Brusius, "Some Reliability Aspects of High Temperature ICs", Fourth International High Temperature Electronics Conference, pp.151-154, Jun. 1998.
- [23] Takahiro Aoki, "A discussion on the Temperature Dependence of Latch-Up Trigger Current in CMOS/BiCMOS Structures", IEEE Transactions on Electron Devices, Vol. 40, No. 11, pp.2023-2028, Nov. 1993.
- [24] B. J. Blalock, "A 1-Volt CMOS Wide Dynamic Range Operational Amplifier", Ph.D Dissertation, School of ECE, Georgia Institute of Technology, Atlanta, GA, 1996.
- [25] P. E. Allen, D. R. Holberg, "CMOS Analog Circuit Design", Oxford University Press, New York, 2002.
- [26] B. Razavi, "Design of Analog CMOS Integrated Circuits", Mc Graw-Hill, 2001.

- [27] D.A. Johns, Ken Martin, "Analog Integrated Circuit Design", John Wiley & Sons, Inc., 1996.
- [28] Joseph N. Babanezhad, "A Rail-to-Rail CMOS Op Amp", IEEE JSSC, Vol. 23, No. 6, pp. 1414 -1417, Dec.1988.
- [29] William C. Black, Jr. et al, "A High Performance Low Power CMOS Channel Filter", IEEE JSSC, Vol. SC-15, No. 6, pp. 929 - 938, Dec. 1980.
- [30] M. J. M. Pelgrom et al, "Matching properties of MOS Transistors", IEEE JSSC, Vol. 24, No. 5, pp. 1433-1440, Oct. 1989.
- [31] T. Pasch et al, "A Low Voltage Differential OpAmp With Novel Common Mode Feedback", IEEE Intl. Conference on Electronics, Circuits and Systems, Vol. 2, pp.345-348, Sep. 1998.
- [32] Mihai Banu et al, "Fully Differential Operational Amplifiers with Accurate Output Balancing", IEEE JSSC, Vol. 23, No. 6, pp.1410-1414, Dec. 1988.
- [33] J. F. Duque-Carrillo, "Continuous-time common-mode feedback networks for fully-differential amplifiers: a comparative study", ISCAS, Vol. 2, pp.1267-1270, May 1993.
- [34] P. M. VanPeteghem et al, "A General Description of Common-Mode Feedback in Fully Differential Amplifiers", ISCAS, pp.3209-3212, May 1990.
- [35] S. Chen, S. Terry, C. Ulaganathan, B. J. Blalock, M. Mojarradi, "A SiGe Current Reference for Low Temperature Analog/Mixed-Signal Applications", 7th Intl. Workshop on Low Temperature Electronics, Netherlands, Jun. 2006.
- [36] Stephen C. Terry, "Low Voltage Analog Circuit Design Using the Adaptively Biased Body-Driven Circuit Technique, Ph.D. Dissertation, University of Tennessee, Knoxville, Aug. 2005.
- [37] T. J. Paulus, J. H. Pierce, "Applied Electronics", Techbooks, 1991.
- [38] SiGe 5am Model Guide.
- [39] Personal Correspondence with Dr. Nance M. Ericsson.
- [40] Personal Correspondence with Tony G. Antonacci and Robert L. Greenwell.
- [41] B. Yashwant Kamath et al, "Relationship Between Frequency Response and Settling Time of Operational Amplifiers", IEEE JSSC, Vol. SC-9, No. 6, pp.347-352, Dec. 1974.

- [42] J. M. Steininger, "Understanding Wide-Band MOS Transistors", IEEE Circuits and Devices, Vol. 6, No. 3, pp. 26-31, Dec. 1990.
- [43] Charles L. Britton, Jr., "Studies On High-Speed Analog Memories for Physics Experiments with Emphasis On Radiation Hardening", Ph.D. Dissertation, University of Tennessee, Knoxville, May 1995.
- [44] Personal Correspondence with Dr. Charles L. Britton.

APPENDIX

A.1 Calculation of Open-loop Gain

The overall gain of the op amp was derived in Section 3.2.1 and is given by the equation (3.17) which is,

$$|A_{V,total}| = |A_{V1}A_{V2}| = g_{m,MP1,2}g_{m,MN8} (r_{o,MP1,MP2} \parallel r_{o,MN1,MN2}) (r_{o,MP10} \parallel r_{o,MN8}) \quad (A.1)$$

The approximate value of the A_{OL} can be estimated from this equation. The transconductance is given by,

$$g_m = \sqrt{2\beta I_D} \quad (A.2)$$

$$g_{m,MP1,2} = \sqrt{2 \times 42 \times 10^{-6} \times \frac{22}{2} \times 20 \times 10^{-6}} = 136 \times 10^{-6} S$$

$$g_{m,MN8} = \sqrt{2 \times 157.2 \times 10^{-6} \times \frac{15 \times 16}{2} \times 160 \times 10^{-6}} = 2460 \times 10^{-6} S$$

The output resistance of each device can be found using,

$$r_o = \frac{1}{\lambda I_D} \quad (A.3)$$

Thus the output impedance of the first stage becomes,

$$r_{o,MP1,MP2} \parallel r_{o,MN1,MN2} = \frac{1}{0.015 \times 20 \times 10^{-6}} \parallel \frac{1}{0.032 \times 20 \times 10^{-6}} \quad (A.4)$$

$$r_{o,IPstage} = 1.064 \times 10^6 \Omega$$

The output impedance of the output stage is,

$$r_{o,MP10} \parallel r_{o,MN8} = \frac{1}{0.015 \times 160 \times 10^{-6}} \parallel \frac{1}{0.032 \times 160 \times 10^{-6}} \quad (A.5)$$

$$r_{o,OPstage} = 133 \times 10^3 \Omega$$

And now the approximate A_{OL} can be found as,

$$A_{V,total} = A_{V1}A_{V2} = 136 \times 10^{-6} \times 2460 \times 10^{-6} \times 1.064 \times 10^6 \times 133 \times 10^3 \quad (A.6)$$

$$A_{V,total} = 47344.25 = 93.5dB$$

A.2 Calculation of Input Referred Noise Voltage

The input referred noise voltage is estimated using equation (3.25) which is included here for convenience.

$$\overline{V_{n,in}^2} = 8kT \left(\frac{2}{3g_{m,MP1}} + \frac{2g_{m,MN1}}{3g_{m,MP1}^2} \right) + \frac{2}{f} \left(\frac{K_N}{C_{OX}W_NL_N} \frac{g_{m,MN1}^2}{g_{m,MP1}^2} + \frac{K_P}{C_{OX}W_PL_P} \right) \quad (A.7)$$

In order to get an estimate for the noise voltage, the value of flicker noise coefficients K_N and K_P need to be determined. These values can be derived using the $1/f$ corner frequency, f_C . Noise analysis simulation was performed on CMOS devices that were configured as common-source amplifiers as shown in Figure A.1 (a) & (b). The f_C depends on the device dimensions and the bias current [26]. So it was important to ensure that the corner frequency got from this simulation was close to that of the op amp's input pair devices of M_{P1} and M_{P2} and the loads of M_{N1} and M_{N2} . Therefore, the device sizes were chosen to be equal to those of the PMOS and NMOS devices in the input stage. Also the identical bias voltages were applied such that the currents were the same. Note that the body of the PMOS device was connected to V_{DD} to maintain equal body effects as well. Thus the corresponding MOSFET devices were matched with those of the input stage, with respect to device size and current. From the noise analysis, the $1/f$ corner frequency of the system in Figure A.1 (a) was found to be 146 KHz and that of

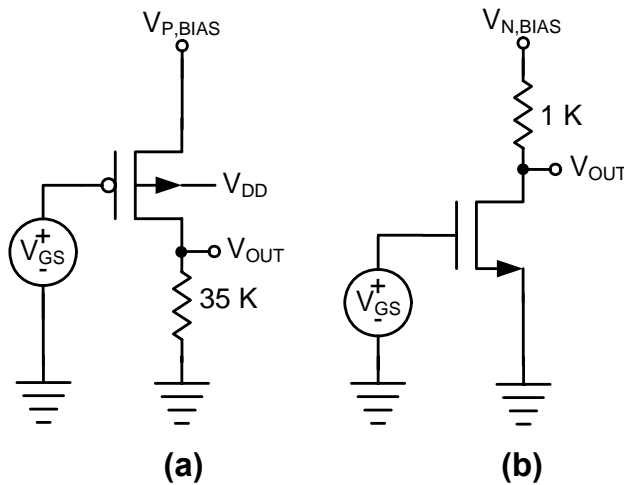


Figure A.1 - Setup to determine the flicker noise corner frequency

Figure A.1 (b) was 1.32 MHz. The flicker noise coefficients were determined using the value of the flicker noise at the corner frequency, as

$$\overline{V_{n,fn}^2} = \frac{K_F}{C_{OX}WL} \times \frac{g_m^2 R_D^2}{f_C} \quad (\text{A.8})$$

For the PMOS device, it is equal to

$$K_{FP} = \overline{V_{n,fn}^2} \frac{C_{OX}WLf_C}{g_m^2 R_D^2} \quad (\text{A.9})$$

$$K_{FP} = \frac{1.74 \times 10^{-15} \times 4.085 \times 10^{-15} \times 22 \times 2 \times 146 \times 10^3}{1.38 \times 10^{-8} \times 1.225 \times 10^9}$$

$$K_{FP} = 2.696 \times 10^{-24} V^2 F$$

Similarly, the flicker noise coefficient of the NMOS device can be determined as,

$$K_{FN} = \frac{3.99 \times 10^{-15} \times 1.9414 \times 10^{-18} \times 8 \times 2 \times 1.32 \times 10^6}{1.8036 \times 10^{-8} \times 1 \times 10^6}$$

$$K_{FN} = 9.076 \times 10^{-24} V^2 F$$

The total input referred noise of the op amp can now be determined. The thermal noise is calculated to be

$$\overline{V_{n,th}^2} = 8kT \left(\frac{2}{3g_{m,MP1}} + \frac{2g_{m,MN1}}{3g_{m,MP1}^2} \right) \quad (\text{A.10})$$

$$\text{where } g_{m,MN1} = \sqrt{2 \times 157.2 \times 10^{-6} \times \frac{8}{2} \times 20 \times 10^{-6}} = 158.59 \times 10^{-6} S \quad (\text{A.11})$$

$$\overline{V_{n,th}^2} = 2 \times 1.656 \times 10^{-20} \left(\frac{2}{3 \times 136 \times 10^{-6}} + \frac{2 \times 158.59 \times 10^{-6}}{3 \times (136 \times 10^{-6})^2} \right)$$

$$V_{n,th} = 18.75 nV_{rms} / \sqrt{Hz}$$

The flicker noise is equal to

$$\overline{V_{n,fn}^2} = \frac{2}{f} \left(\frac{K_{FN}}{C_{OX}W_N L_N} \frac{g_{m,MN1}^2}{g_{m,MP1}^2} + \frac{K_{FP}}{C_{OX}W_P L_P} \right) \quad (\text{A.12})$$

$$\overline{V_{n,fn}^2} = \frac{2}{f} \left(\frac{9.076 \times 10^{-24}}{3.99 \times 10^{-15} \times 8 \times 2} \frac{(158.59 \times 10^{-6})^2}{(136 \times 10^{-6})^2} + \frac{2.696 \times 10^{-24}}{4.085 \times 10^{-24} \times 22 \times 2} \right)$$

$$\overline{V_{n,fn}^2} = \frac{4.164 \times 10^{-10}}{f} V^2 / \text{Hz}$$

At 100 KHz, the input referred flicker noise is

$$\overline{V_{n,fn}^2} = 4.164 \times 10^{-15} V^2 / \text{Hz} \Rightarrow V_{n,fn} = 64.529 \text{ nVrms} / \sqrt{\text{Hz}}$$

Thus the total input referred noise is given by

$$\overline{V_{n,in}^2} = \overline{V_{n,th}^2} + \overline{V_{n,fn}^2} \quad (\text{A.13})$$

$$V_{n,in} = 67.2 \text{ nVrms} / \sqrt{\text{Hz}}$$

A.3 Derivation of the Loop Gain of CMFB Circuit

The loop gain of the common-mode feedback network shown in Figure 3.4 is derived below. The CMFB network is analyzed as two half circuits and the overall gain is computed by superposition of the output signals. Figure A.2 presents the small-signal equivalent of the half-circuit. Applying KCL at node N2, we obtain

$$\begin{aligned} & \mathbf{g}_{m,MP4}(V_{N2} - V_{N1}) + V_{N2} \left(\frac{1}{r_{o,MP4}} + \frac{1}{r_{o,MP5}} + \frac{1}{r_{o,MP6}} \right) + \frac{(V_{N2} - V_{N3})}{r_{o,MP7}} + \mathbf{g}_{m,MP5} V_{N2} \\ & + \mathbf{g}_{m,MP7} V_{N2} = 0 \end{aligned} \quad (\text{A.14})$$

which can be written as

$$\begin{aligned} & \mathbf{g}_{m,MP4}(-V_{N1}) + V_{N2} \left(\mathbf{g}_{m,MP4} + \mathbf{g}_{m,MP5} + \mathbf{g}_{m,MP7} + \frac{1}{r_{o,MP4}} + \frac{1}{r_{o,MP5}} + \frac{1}{r_{o,MP6}} + \frac{1}{r_{o,MP7}} \right) \\ & + \frac{(-V_{N3})}{r_{o,MP7}} = 0 \end{aligned} \quad (\text{A.15})$$

At node N3, applying KCL gives

$$\mathbf{g}_{m,MP7} V_{N2} + \frac{(V_{N2} - V_{N3})}{r_{o,MP7}} = V_{N3} \mathbf{g}_{m,MN3} \quad (\text{A.16})$$

which can be written as

$$V_{N2} \left[\mathbf{g}_{m,MP7} + \frac{1}{r_{o,MP7}} \right] = V_{N3} \left[\mathbf{g}_{m,MN3} + \frac{1}{r_{o,MP7}} \right] \quad (\text{A.17})$$

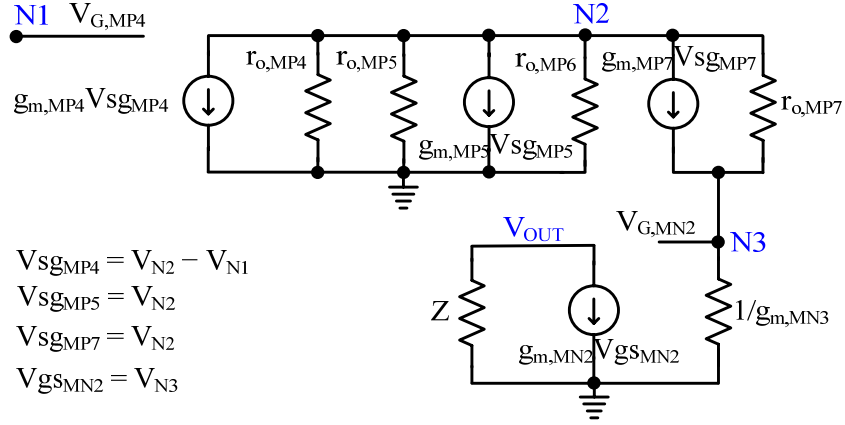


Figure A.2 - Small-signal equivalent of the CMFB's ac half-circuit

At node V_{OUT} , applying KCL gives

$$\frac{V_{OUT}}{Z} + g_{m,MN2}V_{N3} = 0 \quad \Rightarrow \quad V_{N3} = -\frac{V_{OUT}}{g_{m,MN2}Z} \quad (\text{A.18})$$

Substituting the value of V_{N3} from (A.18) in equation (A.17) gives

$$V_{N2} = -\frac{V_{OUT}}{g_{m,MN2}Z} \frac{\left(g_{m,MN3} + \frac{1}{r_{o,MP7}} \right)}{\left(g_{m,MP7} + \frac{1}{r_{o,MP7}} \right)} \quad (\text{A.19})$$

Using (A.18) and (A.19) in (A.15), we get

$$\begin{aligned}
 & -g_{m,MP4}V_{N1} + \frac{V_{OUT}}{Zg_{m,MN2}r_{o,MP7}} - \frac{V_{OUT} \left(g_{m,MN3} + \frac{1}{r_{o,MP7}} \right)}{Zg_{m,MN2} \left(g_{m,MP7} + \frac{1}{r_{o,MP7}} \right)} \times \\
 & \left(g_{m,MP4} + g_{m,MP5} + g_{m,MP7} + \frac{1}{r_{o,MP4}} + \frac{1}{r_{o,MP5}} + \frac{1}{r_{o,MP6}} + \frac{1}{r_{o,MP7}} \right) = 0
 \end{aligned} \quad (\text{A.20})$$

Using $g_{m,MP4} = g_{m,MP5} = \frac{g_{m,MP7}}{2}$, $V_{N1} = V_{IN}$, we get

$$\frac{V_{OUT}}{V_{IN}} = - \frac{g_{m,MP4} g_{m,MN2} Z}{\left(-\frac{1}{r_{o,MP7}} + \frac{\left(g_{m,MN3} + \frac{1}{r_{o,MP7}} \right)}{\left(g_{m,MP7} + \frac{1}{r_{o,MP7}} \right)} \left(4g_{m,MP4} + \frac{4}{r_{o,MP4}} + \frac{1}{r_{o,MP6}} \right) \right)} \quad (\text{A.21})$$

By approximation, the first term in the denominator is very small and can be neglected.

Also, $g_{m,MP4} \gg \frac{1}{r_{o,MP4}} + \frac{1}{r_{o,MP6}}$ and $g_{m,MP7}, g_{m,MN3} \gg \frac{1}{r_{o,MP7}}$. Thus the gain due to the half-circuit becomes

$$\frac{V_{OUT}}{V_{IN}} = - \frac{g_{m,MP4} g_{m,MN2} Z}{2g_{m,MN3}} \quad (\text{A.22})$$

Considering both the half-circuits gives the total gain to be

$$\frac{V_{OUT}}{V_{IN}} = - \frac{g_{m,MP4} g_{m,MN2} (Z_1 + Z_2)}{2g_{m,MN3}} \quad (\text{A.23})$$

where Z_1 and Z_2 are the impedances at the drains of M_{N1} and M_{N2} respectively. At mid-band frequencies, considering $Z_1 = Z_2 = r_{o,MP1} \parallel r_{o,MN1}$, we obtain the loop gain as in equation (3.33) which is

$$A_{CMFB, midband} = \frac{V_{OUT}}{V_{IN}} = - \frac{g_{m,MP4} g_{m,MN2} (r_{o,MP1} \parallel r_{o,MN1})}{g_{m,MN3}} \quad (\text{A.24})$$

A.4 Test Board

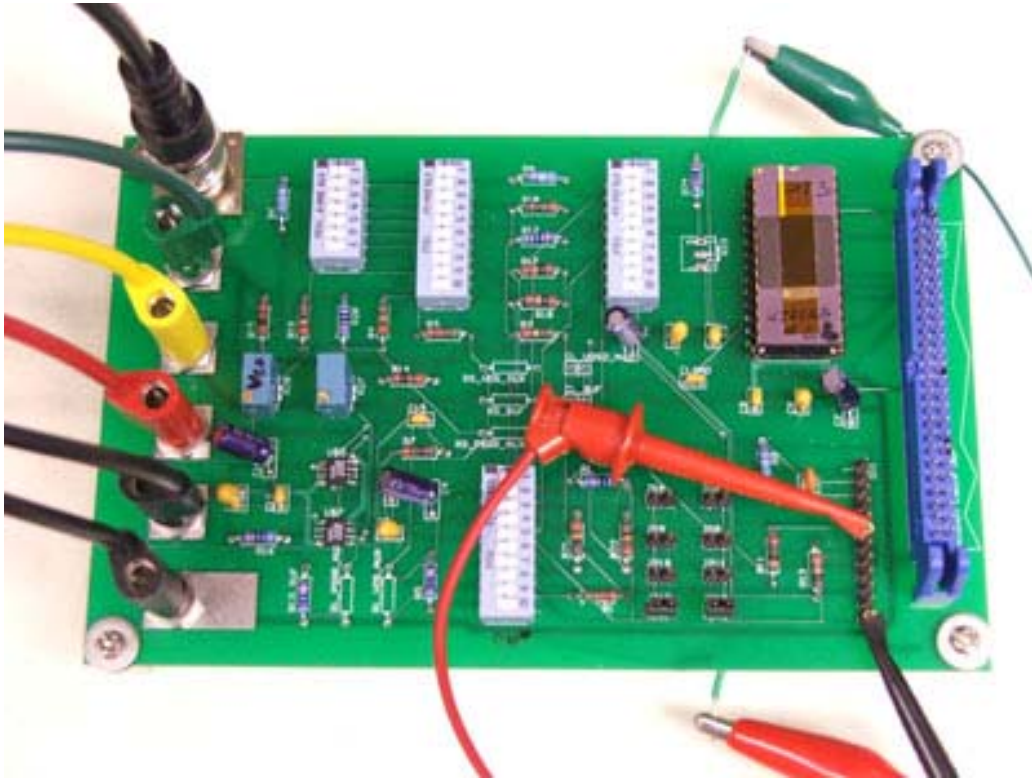


Figure A.3 - Picture of Test Board

VITA

Chandradevi Ulaganathan was born in Pondicherry, India on January 20, 1980. She grew up in Pondicherry and attended the St. Joseph of Cluny Higher Secondary school. She obtained a Bachelor of Technology degree in Electronics and Communication Engineering from Pondicherry University, India in May 2001. Then she worked as a Software Engineer in Infosys Technologies for two years before moving to United States to further her education. She obtained a Master of Science degree in Electrical Engineering from the University of Tennessee, Knoxville in May 2007.